A&A 670, A53 (2023)
https://doi.org/10.1051/0004-6361/202245304


Astronomy & Astrophysics

# Asteroids seen by JWST-MIRI: Radiometric size, distance, and orbit constraints⋆

T. G. Müller[1], M. Micheli[2], T. Santana-Ros[3,4], P. Bartczak[5,6], D. Oszkiewicz[5], and S. Kruk[1]

[1] Max-Planck-Institut für extraterrestrische Physik, Giessenbachstraße, Postfach 1312, 85741 Garching, Germany
e-mail: tmueller@mpe.mpg.de
[2] ESA NEO Coordination Centre, Largo Galileo Galilei, 1, 00044 Frascati (RM), Italy
[3] Departamento de Fisica, Ingeniería de Sistemas y Teoría de la Señal, Universidad de Alicante, Carr. de San Vicente del Raspeig, s/n, 03690 San Vicente del Raspeig, Alicante, Spain
[4] Institut de Ciències del Cosmos (ICCUB), Universitat de Barcelona (IEEC-UB), Carrer de Martí i Franquès, 1, 08028 Barcelona, Spain
[5] Astronomical Observatory Institute, Faculty of Physics, A. Mickiewicz University, Słoneczna 36, 60-286 Poznań, Poland
[6] Instituto Universitario de Física Aplicada a las Ciencias y las Tecnologías (IUFACyT). Universidad de Alicante, Ctra. San Vicente del Raspeig s/n. 03690 San Vicente del Raspeig, Alicante, Spain

Received 27 October 2022 / Accepted 22 November 2022

**ABSTRACT**

Infrared measurements of asteroids are crucial for the determination of physical and thermal properties of individual objects, and for understanding the small-body populations in the solar system as a whole. However, standard radiometric methods can only be applied if the orbit of an object is known, hence its position at the time of the observation. With JWST-MIRI observations the situation will change and many unknown, often very small, solar system objects will be detected. Later orbit determinations are difficult due to the faintness of the objects and the lack of dedicated follow-up concepts. We present MIRI observations of the outer-belt asteroid (10920) 1998 BC1 and an unknown object, detected in all nine MIRI bands in close apparent proximity to (10920). We developed a new method called STM-ORBIT to interpret the multi-band measurements without knowing the object's true location. The power of the new technique is that it determines the most-likely heliocentric and observer-centric distance and phase angle ranges, allowing us to make a radiometric size estimate. The application to the MIRI fluxes of (10920) was used to validate the method. It leads to a confirmation of the known radiometric size-albedo solution, and puts constraints on the asteroid's location and orbit in agreement with its true orbit. To back up the validation of the method, we obtained additional ground-based light curve observations of (10920), combined with *Gaia* data, which indicate a very elongated object ($a/b \geq 1.5$), with a spin-pole at $(\lambda, \beta)_{\rm ecl} = (178°, +81°)$, with an estimated error of about 20°, and a rotation period of $4.861191 \pm 0.000015$ h. A thermophysical study of all available JWST-MIRI and WISE measurements leads to a size of 14.5–16.5 km (diameter of an equal-volume sphere), a geometric albedo $p_{\rm V}$ between 0.05 and 0.10, and a thermal inertia in the range 9–35 (best value 15) J m$^{-2}$ s$^{-0.5}$ K$^{-1}$. For the newly discovered MIRI object, the STM-ORBIT method revealed a size of 100–230 m. The new asteroid must be on a low-inclination orbit ($0.7° < i < 2.0°$) and it was located in the inner main-belt region during JWST observations. A beaming parameter $\eta$ larger than 1.0 would push the size even below 100 meters, a main-belt regime that has escaped IR detections so far. This kind of MIRI observations can therefore contribute to formation and evolution studies via classical size-frequency studies, which are currently limited to objects larger than about one kilometer in size. We estimate that MIRI frames with pointings close to the ecliptic and short integration times of only a few seconds will always include a few asteroids; most of them will be unknown objects.

**Key words.** minor planets, asteroids: general – minor planets, asteroids: individual: (10920) – infrared: planetary systems – techniques: photometric – radiation mechanisms: thermal

## 1. Introduction

The radiometric method is widely used to determine physical and thermal properties of small atmosphereless objects in the Solar System (e.g., Delbo et al. 2015). Measurements in the thermal infrared (IR) are combined with reflected light properties (usually represented by an object's $H$, $G1$, $G2$ values[1]) to find size-albedo solutions that explain the visual magnitudes and the IR fluxes simultaneously. If sufficient good-quality IR measurements are available, it is also possible to determine surface properties, such as roughness, thermal inertia, and thermal conductivity. A detailed modeling of the temperature distribution on the surface even allows us to put constraints on spin or shape properties (e.g., Müller et al. 2017). Different thermal models are available, for example the Standard Thermal Model (STM; Lebofsky et al. 1986), the Near-Earth Thermal Model (NEATM; Harris 1998), or the more complex Thermophysical Model (TPM; Lagerros 1996, 1997, 1998; Rozitis & Green 2011). The STM or NEATM are typically applied to survey data (e.g., Tedesco et al. 2002a,b; Usui et al. 2011; Mainzer et al. 2011), while TPM techniques are used in cases where spin-shape properties are known or for the interpretation of more complex data sets. All of these techniques have in common that they work for objects with known orbits where the heliocentric distance, the observer-centric distance, and the phase angle are known for

⋆ This work is based on observations made with the NASA/ESA/CSA *James Webb* Space Telescope (JWST). The data were obtained from the ESA JWST Science Archive at https://jwst.esac.esa.int/archive/

[1] $H$ is the object's absolute magnitude, $G1$ and $G2$ describe the shape of the phase function (Muinonen et al. 2010).

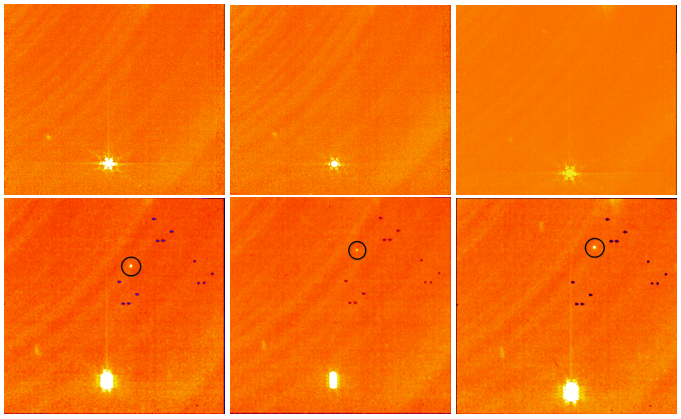

**Fig. 1.** MIRI L3 images of asteroid (10920) (top row) in the $F1000W$, $F1130W$, and $F1280W$ band (from left to right), and in the reference frame of (10920). The JWST-centric position of (10920) is 15h41m21.3s in RA and –19°12′17.0″, the FOV about 50″ × 40″. Bottom row: Corresponding L2 data in the same three bands, but the four dithered images in each band were manually stacked on the new faint asteroid (visible as a faint point source in the upper part of the images, marked with a black circle). The FOV is about 50″ × 50″. The new object is not visible in the standard L3 data products in the archive.

each individual observing epoch. In this context, the JWST asteroid observations and potential science cases are presented and discussed by Norwood et al. (2016), Rivkin et al. (2016), and Thomas et al. (2016), but the scientific aspects of IR detections of unknown object are not well covered yet.

Here, we present JWST-MIRI size and orbit constraints of the outer MBA (10920) 1998 BC1 and a faint, unknown object (Sect. 2). For (10920) we complement the MIRI observations by light curve and *Gaia* DR3 for spin-shape modeling, ATLAS survey data for an estimation of its $H$-magnitude, and WISE observations for a radiometric study. The derived MIRI photometric and astrometric information is given in Sect. 3, followed by a detailed radiometric TPM study for (10920) (Sect. 4). In Sect. 5 we exploit the possibilities and limitations of newly developed STM-ORBIT method for the determination of the object's physical and orbital properties just based on IR data alone. We apply the new method first to the known asteroid (10920) for testing purposes and then to a newly discovered object where no orbit solution is available. The results are discussed in Sect. 6 and summarized in Sect. 7.

## 2. Observations

### 2.1. JWST-MIRI observations

A MIRI imaging mode (Bouchet et al. 2015) multi-filter measurement sequence was executed on July 14, 2022, as part of the JWST calibration program "MIRI Imaging Filter Characterization". The main-belt asteroid (10920) 1998 BC1 was the prime object; however, the individual images also show a faint object that moved with respect to (10920) and the background sources (see Fig. 1). This faint unknown object was in the 56.3″ × 56.3″ field of view (FOV; BRIGHTSKY subarray with 512 × 512 pixels) in all nine MIRI bands, while the much brighter MBA (10920) was found to be located at the edge or even outside the FOV in the long-wavelength measurements. In each of the nine MIRI filters, a set of four dithered images were taken, each with a frame time of 0.865 s (FASTR1 readout mode), and an exposure time of 21.632 s (F0560 band) or 8.653 s (for all other bands). The JWST data processing is done in three different stages[2], using the following pipeline modules for the MIRI imaging observations: `calwebb_detector1` (L1) to process raw ramps data into uncalibrated slopes data (data quality initialization, saturation check, reference pixel correction, jump detection, slope fitting, reset anomaly correction, first-last frame correction, linearity and RSCD[3] correction, dark subtractions); `calwebb_image2` (L2) to process data from uncalibrated slope images into calibrated slope images (WCS[4] information, background subtraction, flat-field correction, flux calibration, drizzle algorithm to produce rectified 2D products); `calwebb_image3` (L3) to process the imaging data from calibrated slope images to mosaics and source catalogs (refine relative WCS, moving target WCS, background matching with Skymatch, outlier detection, image combination, source catalog, update of exposure level products).

For the dedicated (10920) observations presented here, we used the calibrated L2 images (corrected for detector and physical effects, and flux calibrated) where we found four individual (dithered) images per filter (for the astrometry and flux extraction). We also worked with the pipeline-processed calibrated L3 images (see Fig. 1 top row) with the four dithered images combined with respect to the moving target (10920) position, and manually combined L2 images after stacking onto the new object's position (see Fig. 1 bottom row). More details on the MIRI imaging mode can be found in the JWST-specific documentation[5]. Table 1 summarizes details for the 36 individual data frames.

The level 2 (L2) products are absolutely calibrated individual exposures. The level 3 (L3) products have all four dithered images combined (here, stacked on the calculated JWST-centric position of asteroid (10920) 1998 BC1). These L3 images have effective integration times of 86.528 s ($F560W$ band) and 34.612 s (all other bands). Figure 1 shows the F1000$W$, $F1130W$, $F1280W$ L3 images (top row) where the dithered frames were combined (pipeline processed) on the prime target's position. The star-shaped JWST PSF[6] of asteroid (10920) dominates the lower quarter of the frames. The bottom row shows the same data, but now the L2 data are manually stacked on the position of the faint moving object (point source moving up in vertical direction), which can easily be seen in individual dither frames.

### 2.2. Auxiliary observations and light curves for (10920)

Although asteroid (10920) was discovered in 1998, there is very little knowledge about its physical properties. No shape model or full light curves are available, meaning that the spin state of the body is unknown. Since the asteroid's shape and orientation are needed to refine the radiometric model, we performed an observation campaign from August to September 2022 to obtain a light curve of (10920) (see Fig. 2). We used the 2 m telescopes of the Las Cumbres Observatory network: the Faulkes Telescope North (FTN) located at Haleakala Observatory and the Faulkes Telescope South (FTS) at Siding Spring observatory.

[2] https://jwst-docs.stsci.edu/jwst-science-calibration-pipeline-overview/stages-of-jwst-data-processing
[3] Reset Switch Charge Decay.
[4] World Coordinate System; https://fits.gsfc.nasa.gov/fits_wcs.html
[5] https://jwst-docs.stsci.edu/jwst-mid-infrared-instrument/miri-observing-modes/miri-imaging
[6] Point spread function.

**Table 1.** MIRI imaging mode observations of asteroid (10920) 1998 BC1 taken as part of a filter characterization calibration program.

| No. | ID [a] | Date-BEG...END [b] | Filter [c] | $T_{exp}$ (s) [d] |
|---|---|---|---|---|
| 01 | 2101 | 10:21:08.7...10:21:30.4 | F560W | 21.632 |
| 02 | 2101 | 10:24:25.1...10:24:46.8 | F560W | 21.632 |
| 03 | 2101 | 10:27:45.9...10:28:07.5 | F560W | 21.632 |
| 04 | 2101 | 10:31:05.8...10:31:27.4 | F560W | 21.632 |
| 05 | 2103 | 10:36:05.2...10:36:13.8 | F770W | 8.653 |
| 06 | 2103 | 10:39:09.5...10:39:18.1 | F770W | 8.653 |
| 07 | 2103 | 10:42:13.8...10:42:22.4 | F770W | 8.653 |
| 08 | 2103 | 10:45:14.7...10:45:23.3 | F770W | 8.653 |
| 09 | 2105 | 10:50:42.6...10:50:51.2 | F1000W | 8.653 |
| 10 | 2105 | 10:53:46.0...10:53:54.7 | F1000W | 8.653 |
| 11 | 2105 | 10:56:45.2...10:56:53.8 | F1000W | 8.653 |
| 12 | 2105 | 10:59:46.0...10:59:54.7 | F1000W | 8.653 |
| 13 | 2107 | 11:04:14.2...11:04:22.9 | F1130W | 8.653 |
| 14 | 2107 | 11:07:17.7...11:07:26.3 | F1130W | 8.653 |
| 15 | 2107 | 11:10:24.6...11:10:33.3 | F1130W | 8.653 |
| 16 | 2107 | 11:13:26.3...11:13:35.0 | F1130W | 8.653 |
| 17 | 2109 | 11:17:52.0...11:18:00.6 | F1280W | 8.653 |
| 18 | 2109 | 11:20:55.4...11:21:04.0 | F1280W | 8.653 |
| 19 | 2109 | 11:24:00.5...11:24:09.2 | F1280W | 8.653 |
| 20 | 2109 | 11:27:04.9...11:27:13.5 | F1280W | 8.653 |
| 21 | 210B | 11:31:38.3...11:31:47.0 | F1500W | 8.653 |
| 22 | 210B | 11:34:43.5...11:34:52.1 | F1500W | 8.653 |
| 23 | 210B | 11:37:47.8...11:37:56.5 | F1500W | 8.653 |
| 24 | 210B | 11:40:51.2...11:40:59.9 | F1500W | 8.653 |
| 25 [e] | 210D | 11:45:16.9...11:45:25.5 | F1800W | 8.653 |
| 26 | 210D | 11:48:18.6...11:48:27.2 | F1800W | 8.653 |
| 27 | 210D | 11:51:26.4...11:51:35.0 | F1800W | 8.653 |
| 28 | 210D | 11:54:31.5...11:54:40.2 | F1800W | 8.653 |
| 29 [f] | 210F | 11:58:54.6...11:59:03.3 | F2100W | 8.653 |
| 30 | 210F | 12:01:58.0...12:02:06.7 | F2100W | 8.653 |
| 31 [f] | 210F | 12:05:01.5...12:05:10.1 | F2100W | 8.653 |
| 32 [f] | 210F | 12:08:01.4...12:08:10.1 | F2100W | 8.653 |
| 33 [f] | 210H | 12:13:11.3...12:13:19.9 | F2550W | 8.653 |
| 34 [f] | 210H | 12:16:21.6...12:16:30.3 | F2550W | 8.653 |
| 35 [f] | 210H | 12:19:31.1...12:19:39.8 | F2550W | 8.653 |
| 36 [f] | 210H | 12:22:35.4...12:22:44.1 | F2550W | 8.653 |

**Notes.** The calibration proposal ID is 1522. All measurements also include a faint moving source, while the prime target asteroid was in some cases not in the FOV. [a]The official JWST IDs (all starting with V01522002001P000000000). [b]The UT start and end times (all taken on 2022 July 14). [c]The MIRI filter band. [d]The exposure times. [e]PSF of asteroid (10920) is half outside the MIRI image. [f]Asteroid (10920) is outside the FOV.

All light curve data has been submitted to LCDB[7] and can be retrieved by searching for "10920". Figure 2 shows the relevant measurements together with their photometric errors. The scatter between the photometric points is not fully compatible with the photometric errors. However, the viewing geometry changed slightly over the 32 days of measurements (phase angle range from 16.4° to 15.0°). Therefore, the scatter on the composite light curve for observations taken some weeks apart is reasonable and expected for this very elongated object. The light curves are close to a sinusoidal function and show a large amplitude (larger than one magnitude in some cases) and a spin period of about 4.86 h. In order to study the spin shape and orientation we used a modified version of the SAGE modeling technique (Bartczak & Dudziński 2018) to fit our light curve combined with the 13 available *Gaia* DR3[8] sparse photometric measurements of (10920) (Tanga et al. 2022). We used a simple triaxial ellipsoid shape to fit the data since there were not enough measurements to study detailed shape features. However, this simple shape model has proved to work very efficiently when fitting sparse data like those provided by *Gaia* (Cellino et al. 2015), and also combined with ground-based light curves (Santana-Ros et al. 2015). We found a solid pole solution with $\lambda_{ecl} = 178°$ and $\beta_{ecl} = 81°$ (with an estimated error of about 20°), and a very elongated shape with axis ratios of $a/b = 1.5$–$1.8$ and $b/c = 1.0$–$1.1$. The *Gaia* and WISE (see Sect. 2.3 and Fig. B.1) data are best matched by $a/b \approx 1.5$, while ground-based data pointed to an even more extreme elongation of the object. The SAGE light curve inversion (including the fit to the *Gaia* DR3 data) also resulted in a well-determined rotation period of $4.861191 \pm 0.000015$ h. From the spin solution we can infer that the object is always observed close to an equator-on viewing geometry, meaning that the aspect angle will not change much from apparition to apparition. Therefore, changes in the observed cross section of the object are mainly dominated by the a/b axis ratio while the object is rotating. We used the derived simple ellipsoidal spin-shape solution to phase the light curve (Fig. 2) back to the epoch of MIRI observations of (10920) (14 July 2022). The phased light curve shows that MIRI observations were obtained mainly during the minima, implying that most of the measurements were gathered close to the smallest possible cross section of the body; only the long-wavelength bands were taken at higher brightness approaching light curve maximum.

For the determination of the H-magnitude of (10920) we fitted the $H$, $G1$, $G2$ photometric phase function of Muinonen et al. (2010) to the data from the ATLAS survey (Tonry et al. 2018). We utilized only the photometry from the orange filter as it was more numerous and had a better phase angle coverage than the data from the cyan filter. The orange passband (≈550–820 nm) largely covers the Johnsons $V$-band (≈500–700 nm) and the derived $H$ values are very similar[9]. Photometry was downloaded through an astroquery wrapper for querying services at the IAU Minor Planet Center (MPC; Ginsburg et al. 2019). Since the aspect changes between the oppositions are minimal, we fitted the data from three oppositions (2018, 2019–2020, 2021) together (see Fig. 3). The fit was performed in the flux domain using a linear least-squares procedure, and we assumed 0.2 mag photometric uncertainty for the individual data points. Following Penttilä et al. (2016) we constrained the fits to obtain a physically meaningful solution: $H_o = 12.51^{+0.14}_{-0.12}$ mag, and phase-function parameters $G_1 = 0.27^{+0.21}_{-0.17}$, $G_2 = 0.20^{+0.08}_{-0.09}$. This compares very well with the values derived by Mahlke et al. (2021) and with a previous study by Oszkiewicz et al. (2011).

### 2.3. Auxiliary WISE observations for (10920)

The Wide-field Infrared Survey Explorer (WISE; Wright et al. 2010), in 2010, mapped large parts of the sky in four IR bands

[7] Asteroid Lightcurve Data Base at: https://alcdef.org/

[8] *Gaia* Data Release 3, https://www.cosmos.esa.int/web/gaia/dr3

[9] The relation between the Johnson $V$-band $H_V$ and $H_o$ derived from the orange-band ATLAS data is $H_V = 1.01757 \pm 0.00536\, H_o + 0.08286 \pm 0.06104$ (Shevchenko et al. 2022, and private communication for the difference between cyan and orange band relations).

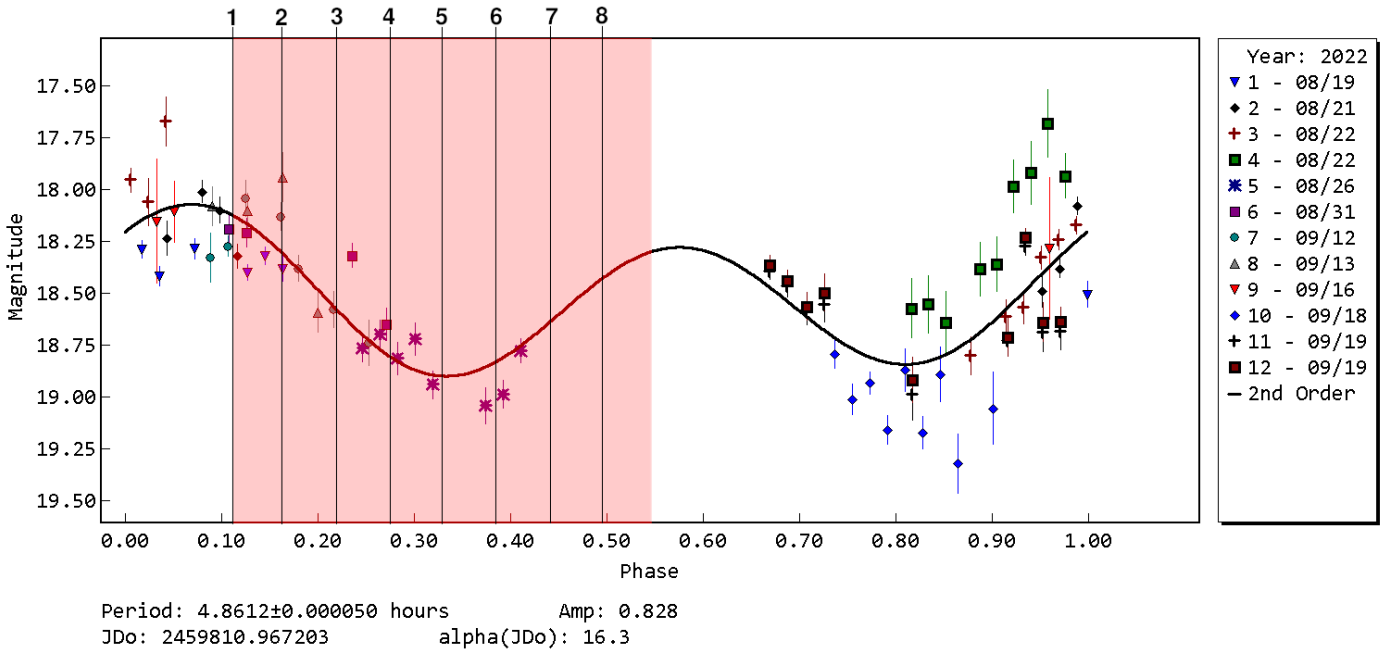


**Fig. 2.** Light curve of (10920) obtained in July–August 2022. Using the period solution, the light curve (in the geocentric reference frame) is phased to the MIRI observation epochs, which are marked with vertical black strokes indicating the beginning of each measurement. The numbers from 1 to 8 correspond to the lines in Table 3.

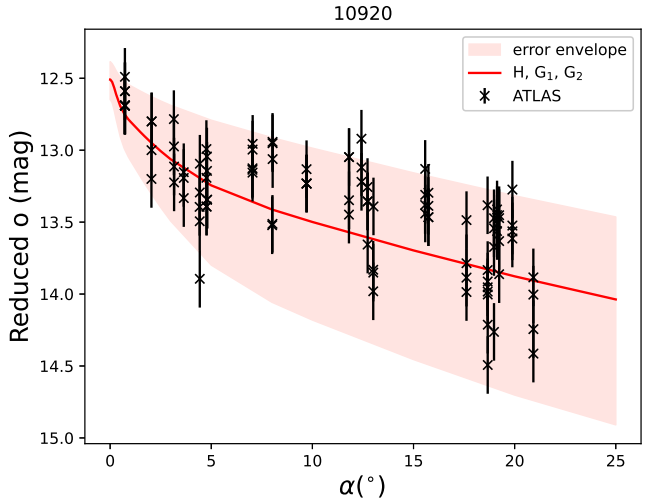


**Fig. 3.** Fitting the $H, G1, G2$ photometric phase function to $o$-band data from the ATLAS survey obtained during three oppositions (2018, 2019–2020, 2021). The single-point uncertainty was assumed to be 0.2 mag.

at 3.4, 4.6, 12, and 22 µm (W1–W4). After the cryo-phase, the mission was continued as Near-Earth Object WISE (NEOWISE; Mainzer et al. 2014), but only in the short-wavelength channels $W1$ and $W2$. Masiero et al. (2011) published a size–albedo solution for (10920) based on multiple $W3$ (15×) and $W4$ (16×) detections. They found a size of $14.436 \pm 0.267$ km and a geometric albedo of $p_V = 0.0847 \pm 0.0159$ (based on $H = 12.50$ mag). The fitted beaming parameter $\eta$ is given with $1.058 \pm 0.038$. Nugent et al. (2015) published a size of $11.12 \pm 2.85$ km and $p_V = 0.11 \pm 0.07$ ($H = 12.80$ mag) as their best solution (via NEATM $\eta$-fit with $\eta = 0.95 \pm 0.17$). Detections from $W1$ (6x) and $W2$ (6×) were used for these calculations. They also found a 0.31 mag amplitude of the WISE 4.6 µm ($W2$) light curve, however, based on only six data points. Mainzer et al. (2019) list another solution where the fit was done on $W2$ (9×), $W3$ (9×), and $W4$ (10×) detections: $D = 15.712 \pm 0.187$ km, $p_V = 0.082 \pm 0.012$, $\eta = 1.087 \pm 0.022$. All WISE-specific radiometric solutions are based on the Near-Earth Asteroid Thermal Model (NEATM; Harris 1998), which uses the beaming parameter $\eta$ to obtain the best fit to the observed spectral slope; $\eta$ depends on the object's rotation, thermal, surface, and emissivity properties, and is also influenced by the observed wavelength regime and observing geometry (heliocentric distance and phase angle). The NEATM is closely connected to the Standard Thermal Model (STM, Lebofsky et al. 1986), which uses a fixed $\eta$ of 0.756, and which is widely applied to main-belt asteroids (e.g., Tedesco et al. 2002a,b; Delbo et al. 2015).

For our radiometric study of asteroid (10920), we extracted all $W2$, $W3$, and $W4$ WISE measurements with photometry quality flags A ($S/N \geq 10$) or B ($3 \leq S/N < 10$), avoiding saturation, moon separation of less than 15° or close-by background sources. The extracted magnitudes were converted to fluxes (see Wright et al. 2010) and color-corrected with correction factors of 1.23, 0.97, and 0.98 for $W2$, $W3$, and $W4$, respectively[10]. For the WISE absolute flux errors we considered the observational flux errors, an estimated error for the color correction, and absolute flux errors that added up to minimum values of 15, 7, and 7% in the $W2$, $W3$, and $W4$ bands, respectively. The full list of WISE fluxes and errors is given in Table B.1.

## 3. MIRI-related results

### 3.1. Astrometry

We determined the PSF centroid of asteroid (10920) (28 L2 images) and the newly discovered object (all 36 L2 images) by

[10] The color correction allows us to produce monochromatic flux densities at the WISE reference wavelengths. These corrections are based on differences between the asteroid's spectral shape compared to the Vega reference spectrum, which was used to establish the WISE photometric calibration.

**Table 2.** The WCS-based RA and Dec coordinates of (10920) and the new object extracted from L2 products via Gaussian centroid fitting to the sources.

| | | (10920) 1998 BC1 | | New object | |
|---|---|---|---|---|---|
| No. | MJD | RA (deg) | Dec (deg) | RA (deg) | Dec (deg) |
| 01 | 59774.431476 | 235.3396411 | –19.2048876 | –19.2049123 | 235.3453320 |
| 02 | 59774.433749 | 235.3395726 | –19.2048763 | –19.2049910 | 235.3454998 |
| 03 | 59774.436073 | 235.3395027 | –19.2048649 | –19.2050717 | 235.3456712 |
| 04 | 59774.438387 | 235.3394330 | –19.2048534 | –19.2051356 | 235.3458419 |
| 05 | 59774.441776 | 235.3393309 | –19.2048367 | –19.2052401 | 235.3460921 |
| 06 | 59774.443910 | 235.3392667 | –19.2048262 | –19.2053028 | 235.3462495 |
| 07 | 59774.446043 | 235.3392024 | –19.2048156 | –19.2053612 | 235.3464069 |
| 08 | 59774.448136 | 235.3391394 | –19.2048053 | –19.2054410 | 235.3465613 |
| 09 | 59774.451932 | 235.3390251 | –19.2047865 | –19.2055228 | 235.3468414 |
| 10 | 59774.454055 | 235.3389612 | –19.2047760 | –19.2055865 | 235.3469981 |
| 11 | 59774.456128 | 235.3388987 | –19.2047658 | –19.2056832 | 235.3471510 |
| 12 | 59774.458222 | 235.3388357 | –19.2047555 | –19.2057778 | 235.3473055 |
| 13 | 59774.461326 | 235.3387422 | –19.2047401 | –19.2058274 | 235.3475346 |
| 14 | 59774.463449 | 235.3386783 | –19.2047296 | –19.2059116 | 235.3476912 |
| 15 | 59774.465613 | 235.3386131 | –19.2047190 | –19.2059585 | 235.3478509 |
| 16 | 59774.467716 | 235.3385498 | –19.2047086 | –19.2060255 | 235.3480061 |
| 17 | 59774.470790 | 235.3384572 | –19.2046934 | –19.2061170 | 235.3482329 |
| 18 | 59774.472913 | 235.3383933 | –19.2046829 | –19.2061859 | 235.3483896 |
| 19 | 59774.475056 | 235.3383288 | –19.2046723 | –19.2062493 | 235.3485477 |
| 20 | 59774.477190 | 235.3382645 | –19.2046618 | –19.2063141 | 235.3487051 |
| 21 | 59774.480355 | 235.3381692 | –19.2046462 | –19.2064240 | 235.3489387 |
| 22 | 59774.482498 | 235.3381047 | –19.2046356 | –19.2064844 | 235.3490968 |
| 23 | 59774.484631 | 235.3380404 | –19.2046250 | –19.2065476 | 235.3492542 |
| 24 | 59774.486754 | 235.3379765 | –19.2046145 | –19.2066109 | 235.3494109 |
| 25 [a] | 59774.489829 | – | – | –19.2067233 | 235.3496377 |
| 26 | 59774.491932 | 235.3378206 | –19.2045890 | –19.2067603 | 235.3497929 |
| 27 | 59774.494105 | 235.3377552 | –19.2045782 | –19.2068342 | 235.3499533 |
| 28 | 59774.496248 | 235.3376906 | –19.2045677 | –19.2069013 | 235.3501114 |
| 29 [b] | 59774.499293 | – | – | –19.2069632 | 235.3503361 |
| 30 | 59774.501416 | 235.3375350 | –19.2045421 | –19.2070349 | 235.3504927 |
| 31 [b] | 59774.503539 | – | – | –19.2070889 | 235.3506494 |
| 32 [b] | 59774.505622 | – | – | –19.2071688 | 235.3508031 |
| 33 [b] | 59774.509208 | – | – | –19.2073011 | 235.3510677 |
| 34 [b] | 59774.511411 | – | – | –19.2073613 | 235.3512302 |
| 35 [b] | 59774.513604 | – | – | –19.2074352 | 235.3513921 |
| 36 [b] | 59774.515738 | – | – | –19.2074973 | 235.3515495 |

**Notes.** MJD is the observation mid-time (UT). [a]Asteroid (10920) at edge, no centroid position possible. [b]Asteroid (10920) is outside FOV.

a simple 2D Gaussian fit, and used the WCS header information to translate the pixel coordinates into a rough estimate of their right ascension (RA) and declination (Dec; see Table 2). The WCS-translated source positions gave a total apparent sky path of 7.27″ in 1:40:42.82 h or an apparent motion of 4.33″ $h^{-1}$, in excellent agreement with JPL/Horizons predictions.

However, the absolute coordinates for (10920) are in poor agreement with the true JWST-centric ephemeris of the object, as determined by JPL/Horizons and our own orbital calculation. They show an offset of about 0.17″, which corresponds to about 1.5 pixels of the MIRI detector. The offset is not aligned with the direction of motion, and is therefore not due to a timing issue.

In order to track down the source of this issue we manually re-measured the position of the asteroid in one of the shorter wavelength images, using stars that are visible in the IR image while still having counterparts in the optical. Unfortunately, only two *Gaia* DR3 sources are contained in the FOV of the MIRI frames. However, we located a deep optical image of the same area of the sky obtained by the Dark Energy Camera (DECam; Flaugher et al. 2015) in their public archive[11]. The frame, dated 2019 February 23, has an exposure time of 56 s, and contains a significant number of optical sources falling close to the MIRI sky-print. We carefully measured the position of 44 such sources versus a *Gaia*-based solution of the entire DECam chip, and used these positions to create a secondary catalog to be applied to the astrometry of the MIRI frame. A total of 16 of these sources showed a detectable counterpart in the MIRI exposure, and could be used to perform a full astrometric solution on it, completely independent from the WCS coefficients. This solution evidenced a bias that exactly compensates the offset observed in the WCS-based astrometry. An astrometric measurement of asteroid (10920) with respect to this self-derived solution fits the existing ephemeris of the asteroid with

[11] https://www.darkenergysurvey.org/the-des-project/data-access/

residuals of <0.01″ in both coordinates (and has a formal uncertainty of roughly ±0.03″). This test proves that the bias we observed in the WCS-based astrometry is due to the WCS solution present in the MIRI images, and it is not a manifestation of a physical offset in the object's true sky position nor of a problem with the ephemeris of the observing spacecraft.

The new object was detected in all 36 L2 frames (nine filters with four dithered frames in each band). The WCS-translated source positions are also given in Table 2. The new target moved by 23.00″ during the 2:01:20.24 h, corresponding to an apparent motion of 11.37″ $h^{-1}$ or about 2.6 times faster than the outer main-belt asteroid (10920). We also determined the absolute astrometric solution for the new object based on the DECam deep optical image and connected to a *Gaia*-based solution, as described above for (10920). This allowed us to determine highly accurate positions (<±0.05″) for the new object in the short-wavelength MIRI bands (where the stars are still visible). The observed arc is in principle too short for the MPC[12] to designate it (it will be kept in the unpublished and unreferenced "Isolated Tracklet File"), but future projects like LSST[13] or the NEO Surveyor[14] might be able to pick it up again. The JWST positions of this new object from July 2022 will then be very useful for orbit calculations.

### 3.2. IR photometry

Before we worked on the flux extraction for both moving objects, we looked at all calibration stars[15] that were observed as part of the MIRI photometric calibration program[16]. They were taken in the same MIRI imaging mode, the same readout (FASTR1) and dither mode (4-POINT-SETS); only the subarray settings (SUB64, SUB128, SUB256, BRIGHTSKY, FULL) and the exposure times were different. These stars cover the MIRI flux range between 0.05 mJy (in F2550W) and above 300 mJy (in F560W), similar to the flux levels of the asteroid (10920). We applied aperture photometry (up to a point where the growth curve flattened out) with the sky background subtracted (calculated within an annulus at a sufficient distance from the star, avoiding background sources and image artifacts). When comparing these aperture fluxes with the corresponding model fluxes[17] (Gordon et al. 2022), we found an agreement of typically 5% or better, but with some outliers on the 10–15% level, mostly in cases where the star was close to the edge of the FOV or near a bright artifact (visible in L2 products). Only for HD 2811 did we find MIRI fluxes (L2 and L3 products) that are about 1.5–2.2 times higher than the model fluxes. The reason for the HD 2811 discrepancy is not clear, but Rieke et al. (2022) flagged this star as less reliable due to obscuration ($A_V > 0.2$ mag). We excluded this star from our study.

Following the experience from our stellar calibration analysis, we performed similar aperture photometry for the two moving objects, both on L2 and L3 data (or manually stacked L2 frames for the new object). For the flux error we considered the scatter between the individual L2 fluxes and the S/N values of the combined images. In case of (10920), the S/N values are well above 100 in all cases and the scatter between fluxes derived from the four L2 frames agrees within 5%. Therefore, we took 5% as the measurement error, except for the single $F2100W$ measurement where a significant part of the source PSF is outside the FOV. Here we performed a half-source photometry (multiplied by 2) and we estimated a 10% measurement error.

For the new object the fluxes are much lower; we note that we used mJy for (10920) and μJy for the new object. Even so, the S/N for this object ranges between 10 and 20 (individual L2 frames) and goes to 25 in some of the final stacked images. At longer wavelengths the object increases in brightness, but the background level also goes up and the detection was more difficult.

The MIRI flux calibration is based on the assumption of $F_{\rm ref}(\lambda)$ = const. (Gordon et al. 2022). It is therefore necessary to color-correct the extracted in-band fluxes to obtain monochromatic flux densities at the MIRI reference wavelengths. Based on the MIRI filter transmission curves and a WISE-based model spectrum for (10920) (Mainzer et al. 2019), we calculated correction factors of 1.15, 1.02, 0.99, 1.00, 0.99, 0.99, 1.00, 1.01, and 1.01 in the nine MIRI bands from $F560W$ to $F2550W$ (roughly corresponding to the corrections for ≈200–240 K blackbodies). For the color correction we assume a 2% error (5% in the F560W band), and for the MIRI absolute flux calibration another 5% error in all bands. All errors were added quadratically. The results are presented in Table 3 and in Figs. 4 and 5. We note that these multi-band fluxes cannot be used to see rotational (light curve) flux variations directly as the flux changes are dominated by the change in wavelength. Only in combination with good-quality spin-shape model solutions is there a possibility to (partially) separate rotational from spectral flux variations (see discussion for (10920) in Sect. 4).

## 4. Radiometric study for MBA (10920)

Figure 4 shows our calibrated MIRI fluxes of MBA (10920) together with two flux predictions. First, a NEATM prediction (blue line) for this specific JWST-centric observing geometry on July 14, 2022. The model parameters ($D$, $p_V$, and $\eta$) are from Mainzer et al. (2019). Second, we calculated a STM prediction ($\eta$=0.756) for a 10 km diameter sphere (with $p_V$=0.082 as in the NEATM calculations) shown in red. The NEATM fluxes are too high (by almost a factor of 2 at 15 μm), while the STM fluxes are in nice agreement in the wavelength range up to 18 μm. Only the 21 μm point is off, but it was taken when the source was at the edge of the MIRI array. As can be seen in Fig. 2, the 21 μm point (No. 8 in Table 3) falls close to the light curve maximum which might also explain the discrepancy with the simple model prediction.

The eight MIRI fluxes (or only seven as the 21 μm flux is uncertain) span a wide wavelength range close to the object's thermal emission peak. We fitted these data with the STM by using different beaming values (and albedos). A beaming parameter of $\eta$ = 0.76 (±0.03) (or 0.73 ± 0.04 when using only seven fluxes) produces the best fit to the observations. In conclusion, the STM assumption with $\eta$ = 0.756 works very well in the case of our MIRI observations of (10920). The corresponding STM radiometric size is 10.0 ± 0.2 km, the geometric albedo 0.13 (assuming an absolute magnitude $H$ = 12.8 mag).

The WISE data were taken in mid-January 2010 (11 detections in W3–W4) at a phase angle of +18.8° (trailing the Sun) and

[12] https://www.minorplanetcenter.net/
[13] https://www.lsst.org/
[14] https://neos.arizona.edu
[15] HD 2811 (subarray mode: SUB64), HD 163466 (SUB64), HD 180609 (SUB128), 2MASS J17430448+6655015 (FULL), 2MASS J18022716+6043356 (BRIGHTSKY), and BD+60-1753 (SUB256)
[16] JWST Calibration program CAL/CROSS 1536.
[17] https://www.stsci.edu/hst/instrumentation/reference-data-for-calibration-and-tools/astronomical-catalogs/calspec

**Table 3.** Extracted MIRI fluxes for the main-belt asteroid (10920) (in mJy) and the new faint asteroid (in μJy).

| | | | MBA (10920) | | | New Object | | |
|---|---|---|---|---|---|---|---|---|
| No. | MJD | $\lambda$ (μm) | flux (mJy) | error[(a)] (mJy) | Comments | flux (μJy) | error[(a)] (μJy) | Comments |
| 1 | 59774.434921 | 5.60 | 0.40 | 0.03 | L2 1-4 & L3 | 4.0 | 1.1 | low S/N |
| 2 | 59774.444966 | 7.70 | 3.89 | 0.27 | L2 5-8 & L3 | 25.9 | 3.4 | |
| 3 | 59774.455084 | 10.00 | 13.19 | 0.90 | L2 9-12 & L3 | 54.3 | 5.7 | |
| 4 | 59774.464526 | 11.30 | 20.14 | 1.48 | L2 13-16 & L3 | 79.7 | 9.0 | |
| 5 | 59774.473988 | 12.80 | 25.67 | 1.63 | L2 17-20 & L3 | 93.5 | 8.3 | |
| 6 | 59774.483560 | 15.00 | 35.83 | 2.15 | L2 21-24 & L3 | 121.3 | 7.5 | |
| 7 | 59774.493029 | 18.00 | 54.31 | 3.98 | L2 26-28 & L3 | 103.1 | 8.3 | high bgr |
| 8 | 59774.502468 | 21.00 | 77.63 | 8.79 | L2 30 & L3 | 91.8 | 24.4 | high bgr |
| 9 | 59774.512490 | 25.50 | – | – | out of FOV | 111.2 | 19.8 | high bgr |

**Notes.** The asteroid (10920) was at a heliocentric distance of r=3.5640 au, a JWST-centric distance of 2.86328 au, a solar elongation of 125.87°, and seen under a phase angle $\alpha$ = 13.51° at observation mid-time (2022-Jul-14 11:20 UT). For the faint new asteroid, only its positions over 2 h and the apparent motion are known (see Table 2). Both objects had a solar elongation ($\lambda - \lambda_{sun}$) = 125.8°, as seen from JWST. [(a)]The flux errors are standard deviations of the photometry of the four L2 images, combined with estimated errors for the color correction and absolute flux calibration.

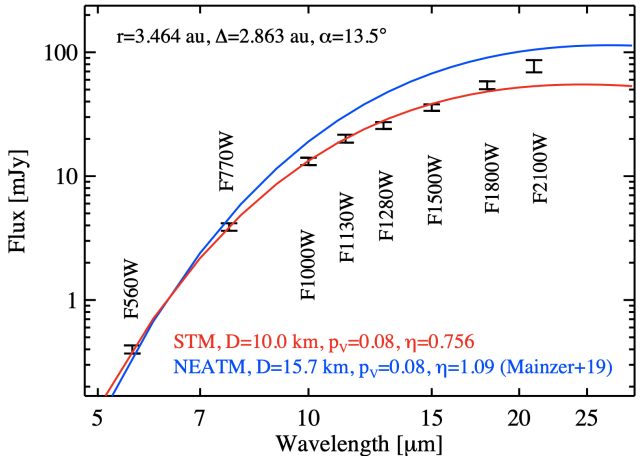


**Fig. 4.** Extracted MIRI fluxes for asteroid (10920), shown together with two different model predictions for the JWST observing epoch and geometry. The blue line shows the NEATM prediction, using the Mainzer et al. (2019) solution; the red line is based on a STM prediction, but using a 10 km diameter for (10920).

in early July 2010 (14 detections in W3–W4) at a phase angle of –17.9° (leading the Sun). These dual-band and dual-epoch data are best fit for a prograde spin of (10920) with a thermal inertia in the range between 9 and 35 J m$^{-2}$ s$^{-0.5}$ K$^{-1}$, with the best-fit value of 15 J m$^{-2}$ s$^{-0.5}$ K$^{-1}$. The WISE flux variations point to an elongated body with an estimated axis ratio $a/b \approx 1.5$ (see Fig. B.1). However, a simple ellipsoidal shape cannot fully explain the observed thermal light curves. Instead, the variations might point to a (contact-)binary system. The relatively high thermal inertia (compared to other outer main-belt objects; see Delbo et al. 2015) leads to a radiometric size of 14.5–16.5 km (the size of an equal-volume sphere), larger than our STM predictions and close to previously published WISE solutions. The best-fit radiometric size for a spherical shape model is 14.7 km; the best fit for the ellipsoidal shape is a bit larger at 15.3 km. Based on the WISE-*W*3 and *W*4 data (Fig. B.1), we estimated a minimum cross section of (10920) of about 10.5 km (similar to our initial STM fit to the JWST data in Fig. 4), and a maximum cross section of 18 km. However, the MIRI observations were taken close to the light curve minimum (see Fig. 2) and a radiometric TPM analysis of these data alone would result in a smaller cross section (about 11–13 km in diameter). Adjusting the MIRI fluxes via our optical light curve data to a light curve-median value (followed by a radiometric study using a spherical model) is not easily possible. Light curves change with phase angle and the interpretation in terms of spin–shape properties depends on surface scattering models (Lu & Jewitt 2019). The IR fluxes, on the other hand, are influenced in a wavelength-dependent fashion by thermally relevant properties, such as surface roughness or thermal inertia (Müller 2002). Only at longer wavelengths, close to the thermal emission peak and beyond, are the thermal fluxes less sensitive to thermal properties and follow closely the object's changes in cross section. A simple (optical) light curve-based correction of the MIRI fluxes is therefore not possible.

The object's albedo is connected to the absolute magnitude. Our measurements (Sect. 2.2) gave a value of $H$ = 12.5 mag, which translates into an albedo of $p_V$ = 0.07. A smaller (larger) $H$-magnitude would lead to a higher (lower) albedo, and $p_V$ values between 0.05 and 0.09 are compatible with the available absolute magnitude fits (see Fig. 3). The low albedo is expected for a typical object in the outer main-belt region (see, e.g., Masiero et al. 2011).

## 5. STM-ORBIT method

In this section, we assume that the orbits of the two asteroids are not known. The goal is to constrain the size, heliocentric distance (at the same time the JWST-centric distance $\Delta$ and the phase angle $\alpha$), and possibly their orbital parameters as well by just using the MIRI fluxes, the JWST-centric RA and Dec coordinates, the derived apparent motion, and the solar-elongation of the targets at the time of the MIRI measurements.

### 5.1. Orbit calculations

For the MBA (10920) we calculated more than 9300 orbits that are compatible with the observed JWST-centric RA and Dec and motion direction of the object, the apparent solar elongation, and the specific apparent motion of 4.33″ h$^{-1}$. The calculations were done via a ranging approach (Virtanen et al. 2001; Oszkiewicz et al. 2009) using the `Find_Orb` software[18]. Similar ranging computations have been used before, but usually

[18] https://www.projectpluto.com/find_orb.htm

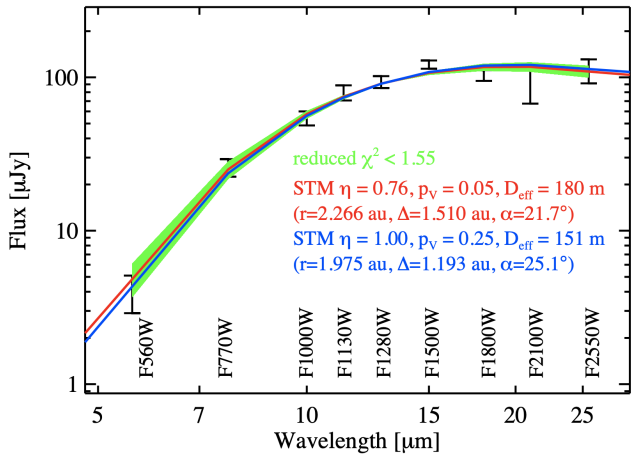


**Fig. 5.** Extracted MIRI fluxes for the new object, shown together with STM predictions for two different $\eta$-values, which also correspond to different best-fit $r, \Delta, \alpha$ observing geometries. The red line shows the $\eta = 0.756$ ($p_V = 0.05$, $D_{\rm eff}$ = km), the blue line the $\eta = 1.0$ ($p_V = 0.25$, $D_{\rm eff}$ = km) STM solution, and the green envelope all orbit solutions with $\chi^2 < 1.55$. The flux scale is given in μJy.

in the context of unconstrained systematic ranging concepts for the orbit determination of near-Earth asteroids, for impact probability calculations, or for collision predictions (e.g., Virtanen & Muinonen 2006; Oszkiewicz et al. 2012; Farnocchia et al. 2015). These orbits cover a wide parameter space with semimajor axes between 0.6 and 1000 au, eccentricities between 0.0 and 1.0, inclinations between 0 and 180°, and perihelion distances from 0.008 to 29 au. All of these orbits can explain the MIRI-specific astrometric data presented in Table 2 within the assumed uncertainties of ±0.025″ and ±0.050″, respectively, for the two objects, with a reduced $\chi^2$ of the orbital fit being close to unity.

For the new asteroid a similar procedure was applied, this time for the specific apparent motion of 11.37″ h$^{-1}$. The almost 10 000 orbits cover a similar parameter space to those for (10920), but due to the different motion of the arc observed in the sky, the orbit ranging approach constrained the orbital perihelia to values below 3.3 au.

Each of the possible orbit solutions comes with orbital parameters $a$ (semimajor axis), $e$ (eccentricity), $i$ (inclination), $q$ (perihelion distance), and the calculated $r_{\rm helio}$ (heliocentric distance [au] from the Sun), $\Delta$ (JWST-asteroid distance [au]), and $\alpha$ (phase angle in [°]) for the specific JWST observing geometry and observing epoch.

### 5.2. STM calculations and fit to the MIRI data

The possible orbit solutions are now taken to calculate flux predictions at the MIRI reference wavelengths, and by using the corresponding $r_{\rm helio}$, $\Delta$, and $\alpha$ values. The model calculations are done via the STM, but with the option of using different values for the beaming parameter $\eta$. A 1 km diameter is used as a starting value and predictions are made for a range of different albedos ($p_V$ = 0.05, 0.10, 0.15, 0.20, and 0.25). In a second step, the reference diameter is scaled up or down to obtain the best fit in terms of $\chi^2$ minimization to the MIRI fluxes. The $\chi^2$ calculation is done via $\sum \frac{(flx_{\rm miri}(i) - flx_{\rm STM}(i))^2}{\sigma(i)^2}$, with $flx_{\rm miri}$ and $\sigma$ being the individual MIRI fluxes and absolute errors (see Table 3), and $flx_{\rm STM}$ the corresponding STM prediction. This recipe produced for each orbit (and each albedo value) the best-fit size solution and the corresponding (reduced) $\chi^2$ value.

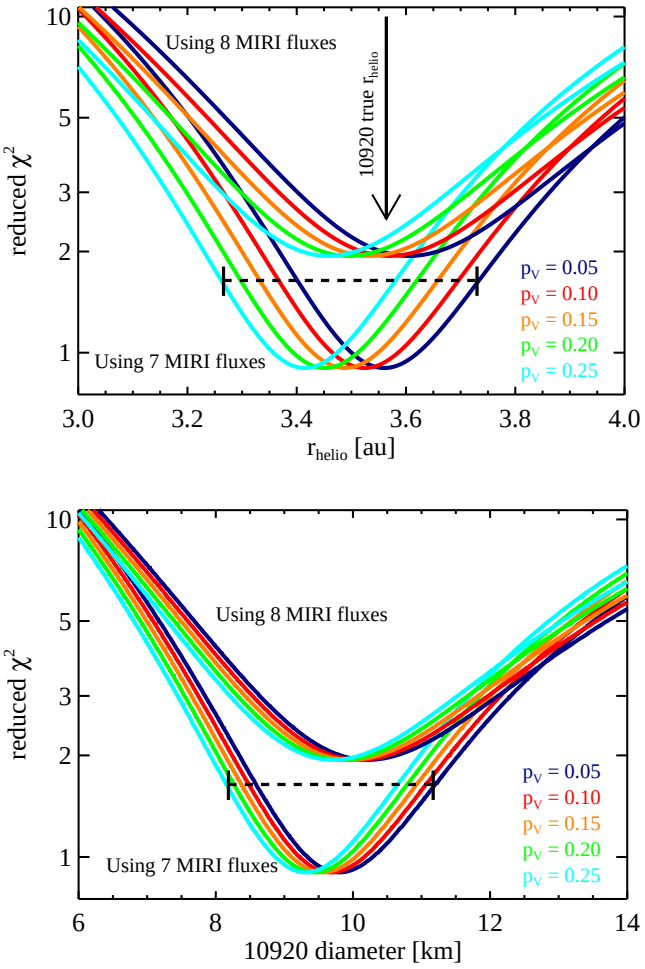


**Fig. 6.** Results of the $\chi^2$ fitting of STM predictions to the measured MIRI fluxes of asteroid (10920). Top: assuming that the orbit of (10920) is not known, the most likely $r_{\rm helio}$ would be in the range between 3.25 and 3.75 au. Bottom: based on the MIRI data alone and assuming a spherical shape of (10920), the most likely size would be in the range between 8 and about 11.5 km.

### 5.3. MBA (10920)

The $\chi^2$ fitting for (10920) was done for all eight fluxes from 5.6 to 21.0 μm (see Table 3), with $\mu = n - m = 7$ as the degree of freedom (considering the diameter scaling as the only fitting parameter $m$). The 21 μm point is not well matched by our spherical STM shape model. The reason could either be that (10920) was partially outside the MIRI FOV and the photometry is simply wrong or that there are spin–shape related problems (see Sect. 2.2). Therefore, we did a separate $\chi^2$ fitting for the seven good-quality fluxes (from 5.6 to 18.0 μm), and with $\mu = 6$ as the degree of freedom for the reduced $\chi^2$ calculations. The results are shown in Fig. 6.

The STM-ORBIT method puts very strong constraints on the object's heliocentric distance at the time of the JWST observations: 3.27 au < $r_{\rm helio}$ < 3.73 au, where the lower (higher) boundary is connected to the assumption of a high (low) albedo of $p_V$ = 0.25 (0.05). This places the object at the edge of the outer main-belt at the time of the JWST observations. In a similar way, the JWST-object distance is limited to 2.56 au < $\Delta_{\rm JWST}$ < 3.04 au, and the phase angle $\alpha$ to values between 13.0 and 14.9°. These derived radiometric distance and angle ranges for (10920)

1998 BC1 are in excellent agreement with the true values $r_{helio}$ = 3.56 au, $\Delta_{JWST}$ = 2.86 au, $\alpha$ = 13.5° at 2022-Jul-14 11:30 UT.

It is interesting that the small observed arc combined with the MIRI fluxes also limits the possible orbital parameters $a$, $e$, $i$, and $q$ (see Fig. A.1): the orbit's semimajor axis $a$ has to be larger than 2.76 au (true value: 3.18 au), the eccentricity $e$ larger than 0.07 (0.15), the inclination $i$ between 0.27° and 0.64° (0.30°), and the perihelion distance between 0.55 au and 3.40 au (2.70 au). This is clearly not sufficient for determining an orbit, but it makes a classification as an outer main-belt object very likely. It seems that we can also exclude highly eccentric orbits ($e > 0.99$) with semimajor axes larger than about 100 au, but here our orbit statistic was not sufficient for a solid confirmation.

The strongest point of the STM-ORBIT method is the size determination. Without knowing the object's true orbit, it is possible to estimate an effective size between 8.2 and 11.2 km, with the smaller value being connected to $p_V = 0.25$ and the larger one to $p_V = 0.05$. The STM-related size is smaller than the radiometric TPM size (see Sect. 4), but this is mainly related to the spherical shape (compared to the extremely elongated shape in the TPM study) and that JWST caught (10920) during the light curve minimum when its cross section is minimal. Constraining the asteroid's albedo is not possible as a bright and large object can produce the same thermal emission as a dark but smaller body.

### 5.4. New asteroid

The $\chi^2$ fitting for the new object was done for all nine fluxes from 5.6 to 25.5 µm (see Table 3), with $\mu = n - m = 8$ as the degree of freedom. The STM-ORBIT method with $\eta = 0.756$, as it was used and verified for the outer MBA (10920), revealed that the new object must be located at a heliocentric distance of about 2.0 – 2.5 au. As smaller objects located closer to the Sun tend to have larger beaming values (see, e.g., discussions in Alí-Lagoa et al. 2016; Alí-Lagoa & Delbo' 2017), we also used $\eta = 1.0$. It turned out that both $\eta$-values can fit the nine fluxes equally well, but the related best-fit heliocentric distances differ (see Fig. 7). To constrain the object's size, location, and orbit, we therefore used the full $\eta$-range from 0.76 to 1.0. Two extreme solutions are shown in Fig. 5: a dark ($p_V = 0.05$, $D_{eff} = 180$ m) object at large heliocentric distance of $r_{helio} = 2.266$ au (red solid line) with a model beaming parameter $\eta = 0.76$, and a bright object ($p_V = 0.25$, $D_{eff} = 151$ m) at $r_{helio} = 1.975$ au (blue solid line), but with a beaming parameter of 1.0. Both solutions fit the MIRI fluxes nicely. All $\chi^2$ compatible solutions (here, for reduced $\chi^2$ values of 1.55) are indicated by the green lines.

The nine MIRI fluxes can then be explained best if the new object is located at $1.73\,\text{au} < r_{helio} < 2.50\,\text{au}$, $0.91\,\text{au} < \Delta_{JWST} < 1.76\,\text{au}$, and $19.2° < \alpha < 29.0°$. The orbital parameters are restricted to $a > 1.3$ au, $e > 0.01$, $0.7° < i < 2.0°$, and $0.1\,\text{au} < q < 2.50\,\text{au}$. This gives a high probability for a low-inclination, inner main-belt object. The size of this newly discovered small body is between 100 m and 230 m in diameter: the smallest value is connected to $\eta = 1.0$ and high albedo; the largest size to $\eta = 0.756$ and a dark albedo. A wide range for the beaming parameters $\eta$ would broaden the parameter range, but due to the very likely inner main-belt location (coming with moderate phase angles below 30°) justifies the applied beaming range. However, an even larger beaming value cannot be excluded and the object would fall into the sub-100 m category, with the heliocentric distance approaching 1.5 au. We also applied the STM-ORBIT method to a reduced observational data set. With less data, the $\chi^2$ goes down and broader parameter ranges (for $r_{helio}$, $D_{eff}$) are compatible with the observations. For example, without the 5.6 µm data point the possible distance from the Sun would slightly decrease to 1.65 au; at the same time, the connected diameter of the new object would shift to 80–220 m. It is therefore essential for the success of the STM-ORBIT method to have detections in the widest possible wavelength range available.

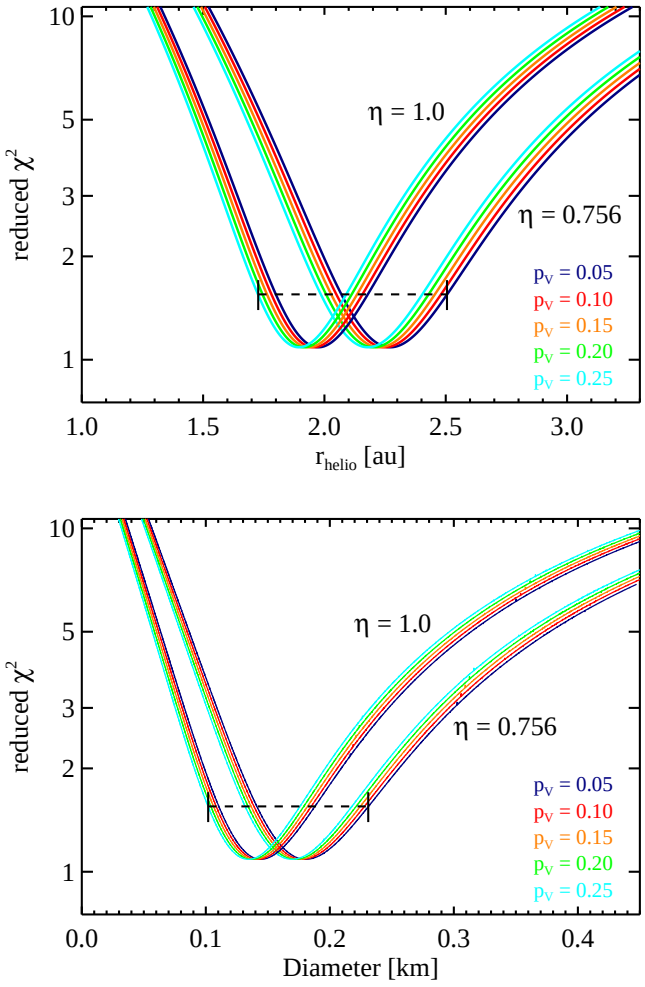


**Fig. 7.** Results of the $\chi^2$ fitting of STM predictions to the measured MIRI fluxes of the new object. The triangles are related to a beaming parameter of $\eta = 1.0$, the diamonds to $\eta = 0.756$. Top: The most likely $r_{helio}$ would be in the range between 1.95 and 2.55 au. Bottom: The most likely size, based on the MIRI data and assuming a spherical shape, would be in the range between 100 and about 230 m.

## 6. Discussion

Our STM-ORBIT method can locate the position ($r_{helio}$, $\Delta$, $\alpha$) of an unknown object and distinguish between a near-Earth object; an inner-, middle-, outer main-belt object; or an object beyond the main belt. Depending on the length of the observed arc, the orbit inclination can also be derived, and strong limitations of the possible perihelion distances can be given. For $a$ and $e$ the method allows us to exclude some extreme cases. However, the big advantage is the radiometric size determination without knowing the object's true orbit. The main uncertainty is related to the poorly constrained beaming parameter $\eta$ and the degeneracy between the object's heliocentric distance and the applied model beaming parameter (see Figs. 5 and 7). As a starting point,

we used the STM default value of $\eta$ = 0.756 (Lebofsky et al. 1986). This is also the best-fit value for (10920) when we use the object's true distances and angles (see Sect. 4). Masiero et al. (2011) used a huge WISE database to determine the beaming parameter of main-belt asteroids as a function of phase angle $\alpha$, $\eta = (0.79 \pm 0.01) + \alpha(0.011 \pm 0.001)$, but with a very large scatter of values between 0.6 and about 2.0. The formula would lead to an $\eta$-value close to 0.95 for (10920) which is too high for our MIRI fluxes. The high-S/N AKARI asteroid measurements (Usui et al. 2011) led to a slightly different correlation of $\eta = (0.76 \pm 0.03) + \alpha(0.009 \pm 0.001)$ (Alí-Lagoa et al. 2018) and about 5% lower beaming values for our case here. Grav et al. (2012) found for the more-distant Hilda group $\eta = 0.85 \pm 0.12$. As the beaming parameter is also influenced by the covered wavelength range (with respect to the object's thermal emission peak), and based on the fit to the (10920) MIRI fluxes, we considered the default STM value a solid starting point for a "blind" interpretation of the MIRI data. For the maximum of $\eta$ we used 1.0, compatible with the above-mentioned published correlations for typical small main-belt objects. However, if an object turns out to be closer to the Sun and/or observed under much larger phase angles, then larger $\eta$-values also have to be considered for the STM-ORBIT method.

For a successful application of the STM-ORBIT method it is also mandatory that the measurements cover a wide wavelength range, or more specifically that the measurements allow us to estimate the object's temperature (in the STM context: the subsolar temperature $T_{SS}$). Already a restriction to the first five filters from 5.6 to 12.8 µm would make the temperature determination more uncertain and enlarge the possible size solutions by almost a factor of 2. In addition, the object location could be anywhere within the main belt. Future projects, such as the NEO Surveyor[19] (Mainzer et al. 2015), plan to measure only in two bands at 4–5.2 µm and 6–10 µm. A similar STM-ORBIT application for newly discovered objects would then only work when multiple time-separated detections in both bands are available.

The unprecedented sensitivity of MIRI guarantees that many small asteroids will be detected. A powerful method to find and extract moving targets from the MIRI imaging data will be the ESASky[20] tool (Racero et al. 2022). The STM-ORBIT method will allow us to determine basic properties and put constraints on their orbits. This is needed in the context of asteroid size–frequency distribution (see, e.g., Bottke et al. 2005, 2015a). Tedesco & Desert (2002) used the ISO satellite (Kessler et al. 1996) to obtain a deep asteroid search at 12 µm in the ecliptic plane. They estimated a cumulative number of MBAs with diameters larger than 1 km between 0.7 and 1.7 million objects. However, the authors also stated that different statistical asteroid models already differ by a factor of two at the 1 km size limit, while at 2 km sizes they are still in good agreement. The MBA statistics at a size range well below 1 km remains unknown. A *Spitzer* (Werner et al. 2004) study by Ryan et al. (2009, 2015) looked into the 0.5–1.0 km diameter asteroid population at different ecliptic latitudes $\beta$ between −17° and +15°. Their IR measurements indicated that the number densities are about a factor of 2–3 below predictions by a standard asteroid model. However, they speculated that the limiting magnitude of current asteroid surveys might have caused the offset. Masiero et al. (2011) presented sizes and albedos of more than 100 000 MBAs derived from the WISE/NEOWISE surveys at thermal IR wavelengths, but with very few exceptions the derived sizes are above 1 km. The mean beaming parameter $\eta$ was found to be about 1.0, ranging from ≈0.94 for small phase angles to values above one at high phases (see also our discussion above about the selection of $\eta$ for our two targets). They confirm a bimodal albedo distribution, and decreasing average albedos when going from the inner main belt to the outer regions. However, due to the WISE detection limits, the subkilometer MBA regime could not be characterized. A recent asteroid study with the *Hubble* Space Telescope (Kruk et al. 2022) found about 60 asteroids per square degree with magnitudes brighter than 24.5 mag in a 30° wide ecliptic band. Size estimates from optical data alone are more difficult, but even the faintest ones are larger than about 200 m.

A main-belt model (Bottke et al. 2015a) predicts about $10^8$ asteroids with sizes of 100 m and larger. If we assume that they are equally distributed over the ecliptic plane (±15°), we find that a typical MIRI image (BRIGHTSKY MIRI subarray with 56.3″ × 56.3″ FOV) will contain on average about two asteroids when pointing towards the ecliptic zone, and even higher numbers directly in the ecliptic plane. However, this number is probably an upper limit as a 100 m object in the middle or outer main-belt will be fainter and more difficult to be seen in MIRI frames. Our two objects seen in the MIRI data from July 14, 2022, seem to match these predictions, but (10920) was the prime target and there is only one obvious serendipitous object. Longer integrations (longer than the 21.6 or 8.7 s per dither position in our case) or more sophisticated search procedures will reveal greater numbers of objects, including smaller and/or more distant objects.

## 7. Conclusions

We present JWST-MIRI fluxes and positions for the outer MBA (10920) and an unknown object in close apparent proximity. The observations were taken in MIRI imaging mode with the BRIGHTSKY subarray on July 14, 2022, between 10:21 and 12:23 UT. Asteroid (10920) was detected in eight bands between 5.6 and 21 µm, and its apparent motion was 4.33″ $h^{-1}$, in perfect agreement with JWST-centric orbit calculations. The new object is visible in all nine MIRI bands, including the 25.5 µm band, and it moved at 11.37″ $h^{-1}$. We combined the MIRI fluxes for (10920) with WISE/NEOWISE observations between 2010 and 2021 and obtained new light curves at visible wavelengths in August and September 2022. Light curve inversion techniques and a radiometric study revealed that (10920) is very elongated (a/b ≥ 1.5), rotates with 4.861191 h, and has a spin-pole at $(\lambda,\beta) = (178°, +81°)$. It has a size of 14.5–16.5 km (the diameter of an equal-volume sphere), a geometric albedo $p_V$ between 0.05 and 0.10, and a thermal inertia in the range 9–35 (best value 15) J $m^{-2}$ $s^{-0.5}$ $K^{-1}$. The albedo and thermal inertia are in good agreement with expectations for C-complex outer MBAs (Delbo et al. 2015).

We used the MIRI positions and fluxes to develop a new STM-ORBIT method that allows us to constrain an object's heliocentric distance at the time of observation and its size without knowing the object's true orbit. The STM-ORBIT technique was tested and validated for (10920) and then applied to the new unknown object. The new object was very likely located in the inner main-belt region at the time of the JWST observations, and it is on a very low-inclination orbit. It has a diameter of 100–230 m, a size range that is very poorly characterized, but very important for size–frequency distribution studies. From a

[19] https://neos.arizona.edu

[20] https://sky.esa.int/esasky/ ESASky was developed by the ESAC Science Data Centre (ESDC) team and maintained alongside other ESA science mission's archives at ESA's European Space Astronomy Centre (ESAC, Madrid, Spain).

size–frequency model by Bottke et al. (2015b) and our experience with the above data, we estimate that typical MIRI images (with a FOV of roughly $1' \times 1'$) will include on average about 1–2 objects with sizes of 100 m or larger when pointed at low ecliptic latitudes. However, the size and location determination for objects without known orbits will only be possible via well-characterized thermal infrared spectra or spectral slopes, preferentially with multi-band detections close to the thermal emission peak.

*Acknowledgements.* TSR acknowledges funding from the NEO-MAPP project (H2020-EU-2-1-6/870377). This work was (partially) funded by the Spanish MICIN/AEI/10.13039/501100011033 and by "ERDF A way of making Europe" by the European Union through grant RTI2018-095076-B-C21, and the Institute of Cosmos Sciences University of Barcelona (ICCUB, Unidad de Excelencia 'María de Maeztu') through grant CEX2019-000918-M. TM would like to thank Víctor Alí-Lagoa for extensive discussion on the beaming parameter $\eta$, Esa Vilenius for his support with the interpretation of $\chi^2$-related statistics, and Karl Gordon for providing information on MIRI photometry. Andras Pal searched through the TESS and Kepler K2 archives for finding more lightcurves for (10920) 1998 BC1, but the asteroid was not covered by these surveys. This publication makes use of data products from the Wide-field Infrared Survey Explorer (WISE), which is a joint project of the University of California, Los Angeles, and the Jet Propulsion Laboratory/California Institute of Technology, and data products from the Near-Earth Object Wide-field Infrared Survey Explorer (NEOWISE), which is a joint project of the Jet Propulsion Laboratory/California Institute of Technology and the University of Arizona. WISE and NEOWISE are funded by the National Aeronautics and Space Administration. This project used public archival data from the Dark Energy Survey (DES). Funding for the DES Projects has been provided by the US Department of Energy, the US National Science Foundation, the Ministry of Science and Education of Spain, the Science and Technology FacilitiesCouncil of the United Kingdom, the Higher Education Funding Council for England, the National Center for Supercomputing Applications at the University of Illinois at Urbana-Champaign, the Kavli Institute of Cosmological Physics at the University of Chicago, the Center for Cosmology and Astro-Particle Physics at the Ohio State University, the Mitchell Institute for Fundamental Physics and Astronomy at Texas A&M University, Financiadora de Estudos e Projetos, Fundação Carlos Chagas Filho de Amparo à Pesquisa do Estado do Rio de Janeiro, Conselho Nacional de Desenvolvimento Científico e Tecnológico and the Ministério da Ciência, Tecnologia e Inovação, the Deutsche Forschungsgemeinschaft, and the Collaborating Institutions in the Dark Energy Survey. A large fraction of this project was conducted during a COVID isolation and quarantine phase of the first author in October 2022. We would like to thank the anonymous reviewer and the editors for their careful reading and very important comments. PPB acknowledges funding through the Spanish Government retraining plan 'María Zambrano 2021-2023' at the University of Alicante (ZAMBRANO22-04).

## References

Alí-Lagoa, V., & Delbo', M. 2017, A&A, 603, A55
Alí-Lagoa, V., Licandro, J., Gil-Hutton, R., et al. 2016, A&A, 591, A14
Alí-Lagoa, V., Müller, T. G., Usui, F., & Hasegawa, S. 2018, A&A, 612, A85
Bartczak, P., & Dudziński, G. 2018, MNRAS, 473, 5050
Bottke, W. F., Durda, D. D., Nesvorný, D., et al. 2005, Icarus, 175, 111
Bottke, W. F., Brož, M., O'Brien, D. P., et al. 2015a, in Asteroids IV, eds. P. Michel, F. DeMeo, & W. Bottke (University of Arizona Press), 701
Bottke, W. F., Vokrouhlický, D., Walsh, K. J., et al. 2015b, Icarus, 247, 191
Bouchet, P., García-Marín, M., Lagage, P. O., et al. 2015, PASP, 127, 612
Cellino, A., Muinonen, K., Hestroffer, D., & Carbognani, A. 2015, Planet. Space Sci., 118, 221
Delbo, M., Mueller, M., Emery, J. P., Rozitis, B., & Capria, M. T. 2015, Asteroid Thermophysical Modeling (Tucson: University of Arizona Press), 107
Farnocchia, D., Chesley, S. R., & Micheli, M. 2015, Icarus, 258, 18
Flaugher, B., Diehl, H. T., Honscheid, K., et al. 2015, AJ, 150, 150
Ginsburg, A., Sipőcz, B. M., Brasseur, C. E., et al. 2019, AJ, 157, 98
Gordon, K. D., Bohlin, R., Sloan, G. C., et al. 2022, AJ, 163, 267
Grav, T., Mainzer, A. K., Bauer, J., et al. 2012, ApJ, 744, 197
Harris, A. W. 1998, Icarus, 131, 291
Kessler, M. F., Steinz, J. A., Anderegg, M. E., et al. 1996, A&A, 315, L27
Kruk, S., García Martín, P., Popescu, M., et al. 2022, A&A, 661, A85
Lagerros, J. S. V. 1996, A&A, 310, 1011
Lagerros, J. S. V. 1997, A&A, 325, 1226
Lagerros, J. S. V. 1998, A&A, 332, 1123
Lebofsky, L. A., Sykes, M. V., Tedesco, E. F., et al. 1986, Icarus, 68, 239
Lu, X.-P., & Jewitt, D. 2019, AJ, 158, 220
Mahlke, M., Carry, B., & Denneau, L. 2021, Icarus, 354, 114094
Mainzer, A., Grav, T., Masiero, J., et al. 2011, ApJ, 736, 100
Mainzer, A., Bauer, J., Cutri, R., et al. 2014, in Lunar and Planetary Science Conference, 45, 2724
Mainzer, A., Grav, T., Bauer, J., et al. 2015, AJ, 149, 172
Mainzer, A. K., Bauer, J. M., Cutri, R. M., et al. 2019, NASA Planetary Data System, https://doi.org/10.26033/18S3-2Z54
Masiero, J. R., Mainzer, A. K., Grav, T., et al. 2011, ApJ, 741, 68
Muinonen, K., Belskaya, I. N., Cellino, A., et al. 2010, Icarus, 209, 542
Müller, T. G. 2002, Meteoritics Planet. Sci., 37, 1919
Müller, T. G., Ďurech, J., Ishiguro, M., et al. 2017, A&A, 599, A103
Norwood, J., Hammel, H., Milam, S., et al. 2016, PASP, 128, 025004
Nugent, C. R., Mainzer, A., Masiero, J., et al. 2015, ApJ, 814, 117
Oszkiewicz, D., Muinonen, K., Virtanen, J., & Granvik, M. 2009, Meteoritics Planet. Sci., 44, 1897
Oszkiewicz, D. A., Muinonen, K., Bowell, E., et al. 2011, J. Quant. Spec. Radiat. Transf., 112, 1919
Oszkiewicz, D., Muinonen, K., Virtanen, J., Granvik, M., & Bowell, E. 2012, Planet. Space Sci., 73, 30
Penttilä, A., Shevchenko, V. G., Wilkman, O., & Muinonen, K. 2016, Planet. Space Sci., 123, 117
Racero, E., Giordano, F., Carry, B., et al. 2022, A&A, 659, A38
Rieke, G. H., Su, K., Sloan, G. C., & Schlawin, E. 2022, AJ, 163, 45
Rivkin, A. S., Marchis, F., Stansberry, J. A., et al. 2016, PASP, 128, 018003
Rozitis, B., & Green, S. F. 2011, MNRAS, 415, 2042
Ryan, E. L., Woodward, C. E., Dipaolo, A., et al. 2009, AJ, 137, 5134
Ryan, E. L., Mizuno, D. R., Shenoy, S. S., et al. 2015, A&A, 578, A42
Santana-Ros, T., Bartczak, P., Michałowski, T., Tanga, P., & Cellino, A. 2015, MNRAS, 450, 333
Shevchenko, V. G., Belskaya, I. N., Slyusarev, I. G., et al. 2022, A&A, 666, A190
Tanga, P., Pauwels, T., Mignard, F., et al. 2022, ArXiv e-prints [arXiv:2206.05561]
Tedesco, E. F., & Desert, F.-X. 2002, AJ, 123, 2070
Tedesco, E. F., Egan, M. P., & Price, S. D. 2002a, AJ, 124, 583
Tedesco, E. F., Noah, P. V., Noah, M., & Price, S. D. 2002b, AJ, 123, 1056
Thomas, C. A., Abell, P., Castillo-Rogez, J., et al. 2016, PASP, 128, 018002
Tonry, J. L., Denneau, L., Heinze, A. N., et al. 2018, PASP, 130, 064505
Usui, F., Kuroda, D., Müller, T. G., et al. 2011, PASJ, 63, 1117
Virtanen, J., & Muinonen, K. 2006, Icarus, 184, 289
Virtanen, J., Muinonen, K., & Bowell, E. 2001, Icarus, 154, 412
Werner, M. W., Roellig, T. L., Low, F. J., et al. 2004, ApJS, 154, 1
Wright, E. L., Eisenhardt, P. R. M., Mainzer, A. K., et al. 2010, AJ, 140, 1868

## Appendix A: Orbital constraints from MIRI data

Here we show the reduced $\chi^2$ values for all possible orbits as a function of the object's semimajor axis $a$, the eccentricity $e$, the inclination $i$, and as a function of the perihelion distance $q$. The orbital constraints are discussed in the main text. The colors represent different albedo values, as in Figs. 6 and 7. Each individual point represents the reduced $\chi^2$ value obtained from the comparison between the MIRI fluxes and the STM-ORBIT-based flux predictions for a given orbit–albedo combination.

### *A.1. MBA (10920) 1998 BC1*

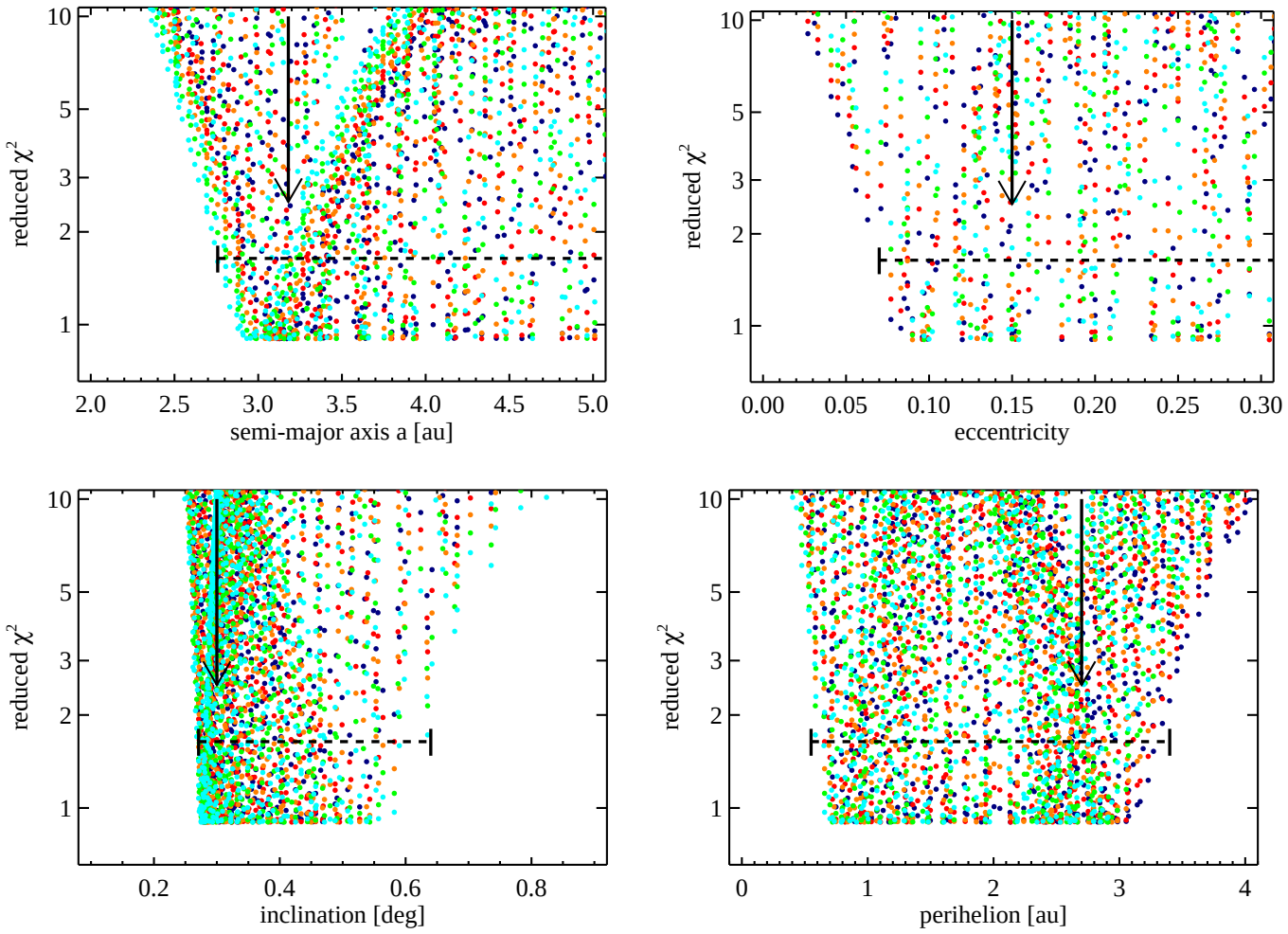


**Fig. A.1.** Orbit constraints from the $\chi^2$ fitting of STM predictions to the measured MIRI fluxes of asteroid (10920). From top to bottom: (i) semimajor axis $a$; (ii) eccentricity; (iii) inclination; (iv) perihelion distance. The true values for the orbit of (10920) are indicated by a vertical arrow. The possible ranges are shown at reduced $\chi^2 = 1.64$ (six degrees of freedom).

### *A.2. New object*

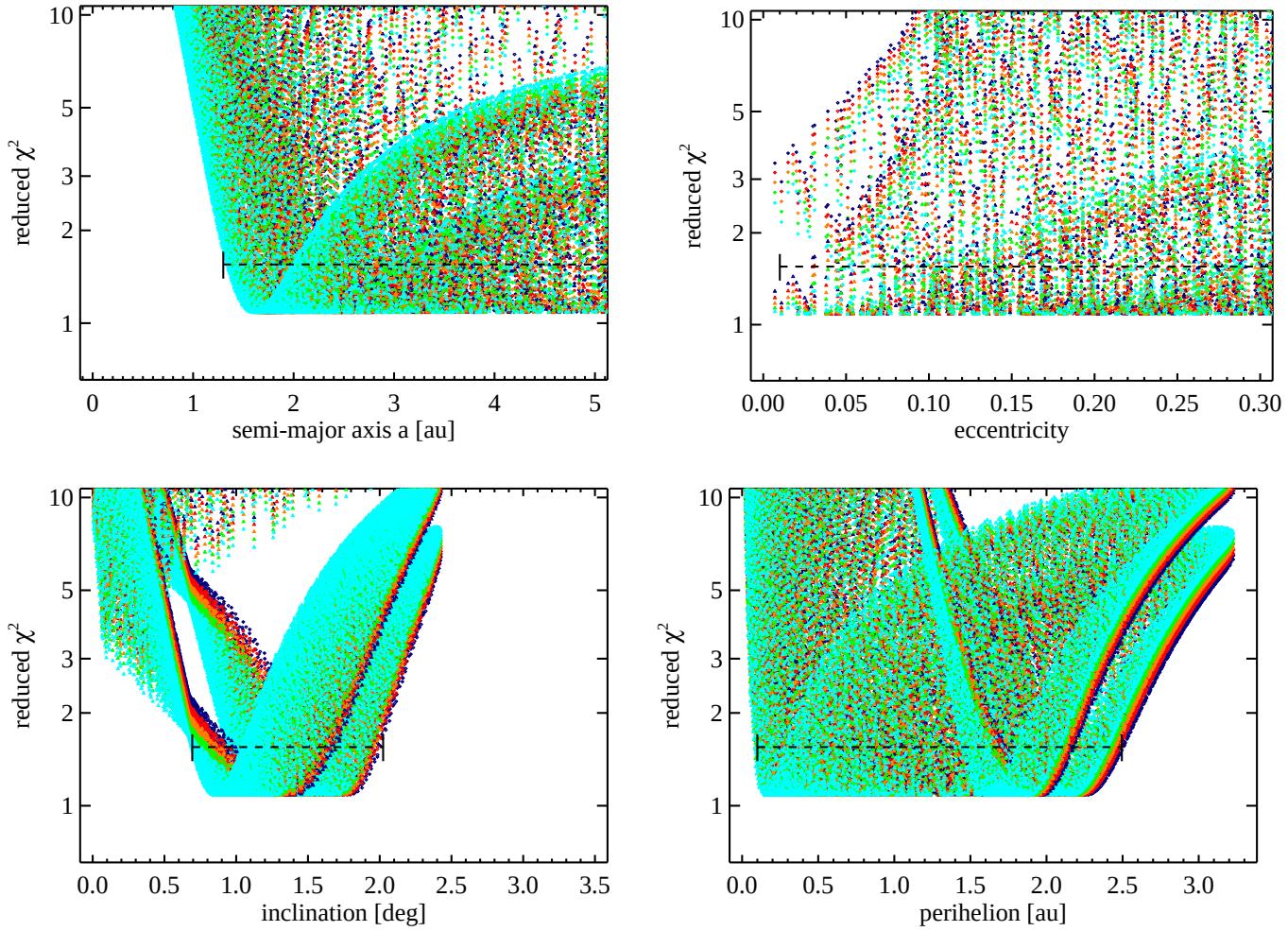


**Fig. A.2.** Orbit constraints from the $\chi^2$ fitting of STM predictions to the measured MIRI fluxes of the new object. From top to bottom: (i) semimajor axis $a$; (ii) eccentricity; (iii) inclination; (iv) perihelion distance. The possible ranges are shown at reduced $\chi^2 = 1.55$ (eight degrees of freedom).

## Appendix B: WISE observations of MBA (10920) 1998 BC1

We extracted all available WISE measurements for (10920) from the different cryogenic and post-cryogenic data sets. The magnitudes were translated into fluxes and color-corrected to obtain monochromatic flux densities at the WISE reference wavelengths. The error calculation is described above. We excluded the WISE W1 band as it is dominated by reflected sunlight for this outer main-belt object.

**Table B.1.** Extracted WISE fluxes for the main-belt asteroid (10920).

| JD[a] | $\lambda$ [μm][b] | flux [mJy][c] | error [mJy][d] | r [au][e] | $\Delta$ [au][f] | $\alpha$ [°][g] | Band[h] | Comments[i] |
|---|---|---|---|---|---|---|---|---|
| 2455211.99146 | 11.10 | 56.043 | 4.070 | 3.0453 | 2.8596 | 18.8 | W3 | A,QFr10 |
| 2455212.12390 | 11.10 | 53.471 | 3.870 | 3.0455 | 2.8579 | 18.8 | W3 | A,QFr10 |
| 2455212.25620 | 11.10 | 26.947 | 2.010 | 3.0457 | 2.8562 | 18.8 | W3 | A,QFr10 |
| 2455212.38851 | 11.10 | 50.877 | 3.682 | 3.0459 | 2.8545 | 18.8 | W3 | A,QFr10 |
| 2455212.45472 | 11.10 | 29.959 | 2.226 | 3.0460 | 2.8536 | 18.8 | W3 | A,QFr10 |
| 2455212.52081 | 11.10 | 59.940 | 4.354 | 3.0461 | 2.8528 | 18.8 | W3 | A,QFr10 |
| 2455212.52094 | 11.10 | 58.307 | 4.207 | 3.0461 | 2.8528 | 18.8 | W3 | A,QFr10 |
| 2455212.58703 | 11.10 | 46.915 | 3.407 | 3.0462 | 2.8519 | 18.8 | W3 | A,QFr10 |
| 2455212.71933 | 11.10 | 62.190 | 4.473 | 3.0464 | 2.8502 | 18.8 | W3 | A,QFr10 |
| 2455212.85176 | 11.10 | 36.385 | 2.652 | 3.0466 | 2.8485 | 18.8 | W3 | A,SAASEP=-3 QFr10 |
| 2455212.98407 | 11.10 | 39.493 | 2.878 | 3.0468 | 2.8468 | 18.8 | W3 | A,QFr10 |
| 2455379.80106 | 11.10 | 32.071 | 2.373 | 3.2857 | 3.0205 | -17.9 | W3 | A,QFr10 |
| 2455379.93336 | 11.10 | 39.095 | 2.859 | 3.2859 | 3.0225 | -17.9 | W3 | A,QFr10 |
| 2455380.06566 | 11.10 | 23.644 | 1.779 | 3.2860 | 3.0245 | -17.9 | W3 | A,QFr10 |
| 2455380.19797 | 11.10 | 26.749 | 2.013 | 3.2862 | 3.0266 | -17.9 | W3 | A,QFr10 |
| 2455380.26406 | 11.10 | 23.973 | 1.796 | 3.2863 | 3.0276 | -17.9 | W3 | A,SAASEP=+10 QFr10 |
| 2455380.33014 | 11.10 | 39.932 | 2.910 | 3.2864 | 3.0286 | -17.9 | W3 | A,SAASEP=+2 QFr10 |
| 2455380.33027 | 11.10 | 39.059 | 2.878 | 3.2864 | 3.0286 | -17.9 | W3 | A,SAASEP=+3 QFr10 |
| 2455380.46245 | 11.10 | 22.936 | 1.726 | 3.2866 | 3.0306 | -17.9 | W3 | A,QFr10 |
| 2455380.46257 | 11.10 | 25.057 | 1.861 | 3.2866 | 3.0306 | -17.9 | W3 | A,QFr10 |
| 2455380.52866 | 11.10 | 37.646 | 2.754 | 3.2867 | 3.0316 | -17.9 | W3 | A,QFr10 |
| 2455380.59475 | 11.10 | 20.518 | 1.573 | 3.2868 | 3.0326 | -17.9 | W3 | A,QFr10 |
| 2455380.66097 | 11.10 | 25.782 | 1.915 | 3.2868 | 3.0336 | -17.9 | W3 | A,QFr10 |
| 2455380.79327 | 11.10 | 19.112 | 1.459 | 3.2870 | 3.0357 | -17.9 | W3 | A,QFr10 |
| 2455380.92557 | 11.10 | 35.952 | 2.660 | 3.2872 | 3.0377 | -17.9 | W3 | A,QFr10 |
| 2455381.05788 | 11.10 | 30.153 | 2.259 | 3.2874 | 3.0397 | -17.9 | W3 | A,QFr10 |
| 2455211.99146 | 22.64 | 163.410 | 12.593 | 3.0453 | 2.8596 | 18.8 | W4 | A,QFr10 |
| 2455212.12390 | 22.64 | 164.770 | 12.698 | 3.0455 | 2.8579 | 18.8 | W4 | A,QFr10 |
| 2455212.25620 | 22.64 | 92.572 | 7.245 | 3.0457 | 2.8562 | 18.8 | W4 | A,QFr10 |
| 2455212.38851 | 22.64 | 149.307 | 11.450 | 3.0459 | 2.8545 | 18.8 | W4 | A,QFr10 |
| 2455212.45472 | 22.64 | 96.579 | 8.613 | 3.0460 | 2.8536 | 18.8 | W4 | A,QFr10 |
| 2455212.52081 | 22.64 | 166.755 | 12.494 | 3.0461 | 2.8528 | 18.8 | W4 | A,QFr10 |
| 2455212.52094 | 22.64 | 184.536 | 14.759 | 3.0461 | 2.8528 | 18.8 | W4 | A,QFr10 |
| 2455212.58703 | 22.64 | 140.243 | 11.216 | 3.0462 | 2.8519 | 18.8 | W4 | A,QFr10 |
| 2455212.71933 | 22.64 | 178.024 | 13.789 | 3.0464 | 2.8502 | 18.8 | W4 | A,QFr10 |
| 2455212.85176 | 22.64 | 114.942 | 9.809 | 3.0466 | 2.8485 | 18.8 | W4 | A,SAASEP=-3 QFr10 |
| 2455212.98407 | 22.64 | 122.484 | 10.022 | 3.0468 | 2.8468 | 18.8 | W4 | A,QFr10 |
| 2455379.80106 | 22.64 | 122.710 | 9.869 | 3.2857 | 3.0205 | -17.9 | W4 | A,QFr10 |
| 2455379.93336 | 22.64 | 123.617 | 9.434 | 3.2859 | 3.0225 | -17.9 | W4 | A,QFr10 |
| 2455380.06566 | 22.64 | 82.886 | 6.782 | 3.2860 | 3.0245 | -17.9 | W4 | A,QFr10 |
| 2455380.19797 | 22.64 | 96.135 | 8.359 | 3.2862 | 3.0266 | -17.9 | W4 | A,QFr10 |
| 2455380.26406 | 22.64 | 78.719 | 7.204 | 3.2863 | 3.0276 | -17.9 | W4 | A,SAASEP=+10 QFr10 |
| 2455380.33014 | 22.64 | 122.710 | 9.760 | 3.2864 | 3.0286 | -17.9 | W4 | A,SAASEP=+2 QFr10 |
| 2455380.33027 | 22.64 | 126.148 | 10.833 | 3.2864 | 3.0286 | -17.9 | W4 | A,SAASEP=+3 QFr10 |
| 2455380.46245 | 22.64 | 80.627 | 7.010 | 3.2866 | 3.0306 | -17.9 | W4 | A,QFr10 |
| 2455380.46257 | 22.64 | 75.942 | 6.950 | 3.2866 | 3.0306 | -17.9 | W4 | A,QFr10 |
| 2455380.52866 | 22.64 | 131.486 | 9.987 | 3.2867 | 3.0316 | -17.9 | W4 | A,QFr10 |
| 2455380.59475 | 22.64 | 75.107 | 6.370 | 3.2868 | 3.0326 | -17.9 | W4 | A,QFr10 |
| 2455380.66097 | 22.64 | 79.374 | 7.554 | 3.2868 | 3.0336 | -17.9 | W4 | A,QFr10 |
| 2455380.79327 | 22.64 | 67.746 | 6.321 | 3.2870 | 3.0357 | -17.9 | W4 | A,QFr10 |
| 2455380.92557 | 22.64 | 128.493 | 10.513 | 3.2872 | 3.0377 | -17.9 | W4 | A,QFr10 |

*continued on next page*

**Table B.1.** *continued*

| JD[a] | $\lambda$ [μm][b] | flux [mJy][c] | error [mJy][d] | r [au][e] | $\Delta$ [au][f] | $\alpha$ [°][g] | Band[h] | Comments[i] |
|---|---|---|---|---|---|---|---|---|
| 2455381.05788 | 22.64 | 102.443 | 8.382 | 3.2874 | 3.0397 | -18.0 | W4 | A,QFr10 |
| 2455211.99146 | 4.60 | 0.299 | 0.072 | 3.0453 | 2.8596 | 18.8 | W2 | ISU,B,QFr10 |
| 2455212.45472 | 4.60 | 0.139 | 0.050 | 3.0460 | 2.8536 | 18.8 | W2 | ISU,B,QFr10 |
| 2455212.52081 | 4.60 | 0.146 | 0.052 | 3.0461 | 2.8528 | 18.8 | W2 | ISU,B,QFr10 |
| 2455212.52094 | 4.60 | 0.297 | 0.068 | 3.0461 | 2.8528 | 18.8 | W2 | ISU,B,QFr10 |
| 2455212.58703 | 4.60 | 0.171 | 0.053 | 3.0462 | 2.8519 | 18.8 | W2 | ISU,B,QFr10 |
| 2455212.71933 | 4.60 | 0.167 | 0.049 | 3.0464 | 2.8502 | 18.8 | W2 | ISU,B,QFr10 |
| 2455379.93336 | 4.60 | 0.277 | 0.063 | 3.2859 | 3.0225 | -17.9 | W2 | ISU,B,QFr10 |
| 2455380.33027 | 4.60 | 0.221 | 0.063 | 3.2864 | 3.0286 | -17.9 | W2 | ISU,B,SAASEP=+3 QFr10 |
| 2456674.91650 | 4.60 | 0.257 | 0.084 | 2.8588 | 2.6455 | -20.1 | W2 | NIS,B,QFr5 |
| 2456675.04830 | 4.60 | 0.198 | 0.063 | 2.8587 | 2.6472 | -20.1 | W2 | NIS,B,QFr10 |
| 2456675.31176 | 4.60 | 0.214 | 0.059 | 2.8583 | 2.6505 | -20.1 | W2 | NIS,B,QFr10 |
| 2456675.31189 | 4.60 | 0.217 | 0.058 | 2.8583 | 2.6505 | -20.1 | W2 | NIS,B,QFr10 |
| 2456675.64118 | 4.60 | 0.219 | 0.061 | 2.8580 | 2.6547 | -20.1 | W2 | NIS,B,QFr10 |
| 2456675.90477 | 4.60 | 0.215 | 0.077 | 2.8576 | 2.6580 | -20.1 | W2 | NIS,B,QFr10 |
| 2456676.03657 | 4.60 | 0.297 | 0.070 | 2.8575 | 2.6597 | -20.1 | W2 | NIS,B,QFr10 |
| 2456974.42707 | 4.60 | 0.438 | 0.102 | 2.7188 | 2.5230 | 21.4 | W2 | NIS,B,QFr5 |
| 2456974.55848 | 4.60 | 0.449 | 0.106 | 2.7188 | 2.5213 | 21.3 | W2 | NIS,B,QFr10 |
| 2456974.55861 | 4.60 | 0.331 | 0.093 | 2.7188 | 2.5213 | 21.3 | W2 | NIS,B,QFr10 |
| 2456974.82156 | 4.60 | 0.315 | 0.101 | 2.7189 | 2.5179 | 21.3 | W2 | NIS,B,QFr10 |
| 2456974.95297 | 4.60 | 0.718 | 0.194 | 2.7190 | 2.5162 | 21.3 | W2 | NIS,B,QFr10 |
| 2456975.15022 | 4.60 | 1.671 | 0.361 | 2.7191 | 2.5136 | 21.3 | W2 | NIS,B,QFr10 |
| 2456977.97713 | 4.60 | 0.521 | 0.094 | 2.7202 | 2.4770 | 21.3 | W2 | NIS,B,QFr5 |
| 2456978.37162 | 4.60 | 0.364 | 0.091 | 2.7203 | 2.4719 | 21.3 | W2 | NIS,B,QFr10 |
| 2456978.50304 | 4.60 | 0.325 | 0.071 | 2.7204 | 2.4702 | 21.3 | W2 | NIS,B,QFr10 |
| 2456978.56874 | 4.60 | 0.327 | 0.075 | 2.7204 | 2.4694 | 21.3 | W2 | NIS,B,QFr10 |
| 2456978.70028 | 4.60 | 0.369 | 0.082 | 2.7205 | 2.4677 | 21.3 | W2 | NIS,B,QFr10 |
| 2456978.76599 | 4.60 | 0.276 | 0.063 | 2.7205 | 2.4668 | 21.3 | W2 | NIS,B,QFr10 |
| 2456978.83170 | 4.60 | 0.193 | 0.059 | 2.7205 | 2.4660 | 21.3 | W2 | NIS,B,QFr10 |
| 2456979.09465 | 4.60 | 0.391 | 0.095 | 2.7206 | 2.4626 | 21.3 | W2 | NIS,B,QFr5 |
| 2456979.22619 | 4.60 | 0.341 | 0.071 | 2.7207 | 2.4609 | 21.2 | W2 | NIS,B,QFr10 |
| 2457138.42474 | 4.60 | 0.394 | 0.095 | 2.8500 | 2.4988 | -20.4 | W2 | NIS,B,QFr10 |
| 2457141.57509 | 4.60 | 0.258 | 0.069 | 2.8537 | 2.5436 | -20.5 | W2 | NIS,B,QFr10 |
| 2457141.57522 | 4.60 | 0.246 | 0.085 | 2.8537 | 2.5436 | -20.5 | W2 | NIS,B,QFr10 |
| 2457141.96895 | 4.60 | 0.243 | 0.073 | 2.8541 | 2.5492 | -20.5 | W2 | NIS,B,QFr5 |
| 2457142.23152 | 4.60 | 0.262 | 0.078 | 2.8544 | 2.5530 | -20.5 | W2 | NIS,B,QFr5 |
| 2457142.69095 | 4.60 | 0.189 | 0.061 | 2.8550 | 2.5596 | -20.5 | W2 | NIS,B,QFr10 |
| 2458725.70223 | 4.60 | 0.217 | 0.061 | 2.8861 | 2.6835 | 20.5 | W2 | NIS,B,QFr10 |
| 2458725.96379 | 4.60 | 0.233 | 0.064 | 2.8858 | 2.6797 | 20.5 | W2 | NIS,B,QFr10 |
| 2458726.09469 | 4.60 | 0.224 | 0.076 | 2.8856 | 2.6778 | 20.5 | W2 | NIS,B,QFr10 |
| 2458726.16014 | 4.60 | 0.295 | 0.085 | 2.8855 | 2.6768 | 20.5 | W2 | NIS,B,QFr10 |
| 2458726.22547 | 4.60 | 0.288 | 0.079 | 2.8854 | 2.6759 | 20.5 | W2 | NIS,B,QFr5 |
| 2458726.42182 | 4.60 | 0.224 | 0.067 | 2.8852 | 2.6730 | 20.5 | W2 | NIS,B,QFr5 |
| 2458726.81428 | 4.60 | 0.226 | 0.075 | 2.8847 | 2.6674 | 20.5 | W2 | ISC,B,QFr5 |
| 2458726.94505 | 4.60 | 0.230 | 0.074 | 2.8845 | 2.6655 | 20.5 | W2 | NIS,B,QFr5 |
| 2458875.40095 | 4.60 | 0.464 | 0.085 | 2.7412 | 2.2133 | -19.4 | W2 | NIS,B,QFr10 |
| 2458875.53185 | 4.60 | 0.315 | 0.073 | 2.7411 | 2.2149 | -19.4 | W2 | NIS,B,QFr10 |
| 2458875.66263 | 4.60 | 0.175 | 0.056 | 2.7411 | 2.2164 | -19.5 | W2 | NIS,B,QFr10 |
| 2458875.79340 | 4.60 | 0.285 | 0.068 | 2.7410 | 2.2180 | -19.5 | W2 | NIS,B,QFr10 |
| 2458875.85885 | 4.60 | 0.213 | 0.067 | 2.7409 | 2.2187 | -19.5 | W2 | NIS,B,QFr10 |
| 2458875.92418 | 4.60 | 0.504 | 0.102 | 2.7409 | 2.2195 | -19.5 | W2 | NIS,B,QFr10 |
| 2458875.92431 | 4.60 | 0.500 | 0.091 | 2.7409 | 2.2195 | -19.5 | W2 | NIS,B,QFr5 |
| 2458875.98912 | 4.60 | 0.230 | 0.076 | 2.7408 | 2.2203 | -19.5 | W2 | NIS,B,QFr10 |
| 2458876.12053 | 4.60 | 0.449 | 0.080 | 2.7408 | 2.2219 | -19.5 | W2 | NIS,A,QFr10 |
| 2458876.25131 | 4.60 | 0.353 | 0.072 | 2.7407 | 2.2234 | -19.5 | W2 | NIS,B,QFr10 |
| 2458876.38209 | 4.60 | 0.236 | 0.062 | 2.7406 | 2.2250 | -19.6 | W2 | ISC,B,QFr10 |
| 2459199.33575 | 4.60 | 0.319 | 0.070 | 2.8360 | 2.6434 | 20.3 | W2 | NIS,B,QFr5 |
| 2459199.46653 | 4.60 | 0.190 | 0.063 | 2.8362 | 2.6417 | 20.3 | W2 | NIS,B,QFr5 |

*continued on next page*

**Table B.1.** *continued*

| JD[a] | $\lambda$ [μm][b] | flux [mJy][c] | error [mJy][d] | r [au][e] | Δ [au][f] | $\alpha$ [°][g] | Band[h] | Comments[i] |
|---|---|---|---|---|---|---|---|---|
| 2459199.85886 | 4.60 | 0.311 | 0.079 | 2.8366 | 2.6367 | 20.3 | W2 | NIS,B,SAASEP=+0 QFr5 |
| 2459199.92418 | 4.60 | 0.220 | 0.065 | 2.8367 | 2.6359 | 20.3 | W2 | NIS,B,SAASEP=-6 QFr10 |
| 2459200.05445 | 4.60 | 0.265 | 0.076 | 2.8368 | 2.6343 | 20.3 | W2 | NIS,B,QFr10 |
| 2459200.31651 | 4.60 | 0.253 | 0.069 | 2.8371 | 2.6309 | 20.3 | W2 | NIS,B,QFr10 |
| 2459200.44728 | 4.60 | 0.241 | 0.065 | 2.8373 | 2.6293 | 20.3 | W2 | NIS,B,QFr10 |
| 2459200.57806 | 4.60 | 0.255 | 0.063 | 2.8374 | 2.6276 | 20.3 | W2 | NIS,B,QFr5 |
| 2459348.02845 | 4.60 | 0.172 | 0.049 | 3.0301 | 2.4990 | -18.0 | W2 | NIS,B,QFr5 |

[a] Observation epoch (Julian date); [b] reference wavelength in the given bands (in $\mu$m); [c] color-corrected, monochromatic flux densities at the reference wavelength (in mJy); [d] absolute flux errors (in mJy); [e] heliocentric distance r (in au); [f] observer–object distance (au); [g] phase angle (in °); [h] band name; [i] quality comments: all measurements were not saturated and had photometry quality flags A (S/N≥10) or B (3≤S/N<10). Cases with South Atlantic Anomaly (SAA) separations ≤10° are flagged. Only quality frame (QFr) scores 5 or 10 were accepted. For the W2 detections we also listed the WISE catalog comments NIS (No Inertial Source), ISU (Inertial Source Undecided), or ISC (Inertial Source Contamination).

With the current spin-shape solution it is unfortunately not possible to combine all data over 12 years as the rotation period is not known with sufficient quality. However, the high-S/N WISE W3 and W4 data from January and July 2010 can be phased very well. They show a strong rotational variation (see Fig. B.1), perfectly consistent with the light curve-derived rotation period. These flux changes are explained by an ellipsoidal shape model with a/b ≈ 1.5. The dual-band data are nicely balanced before and after opposition. The radiometric study resulted in a thermal inertia of 15 J m$^{-2}$s$^{-0.5}$K$^{-1}$, which allows us to unify the observation-to-model ratio for the two bands, and all before and after opposition data from 2010 (reduced $\chi^2$ close to unity). The best-fit sizes are 14.7 km for the spherical shape and 15.3 km for the ellipsoidal model (the size of an equal-volume sphere). The ellipsoidal spin-shape solution was also used for the JWST observations, with a rotational phasing directly connected to our 2022 light curve measurements (see Fig. 2).

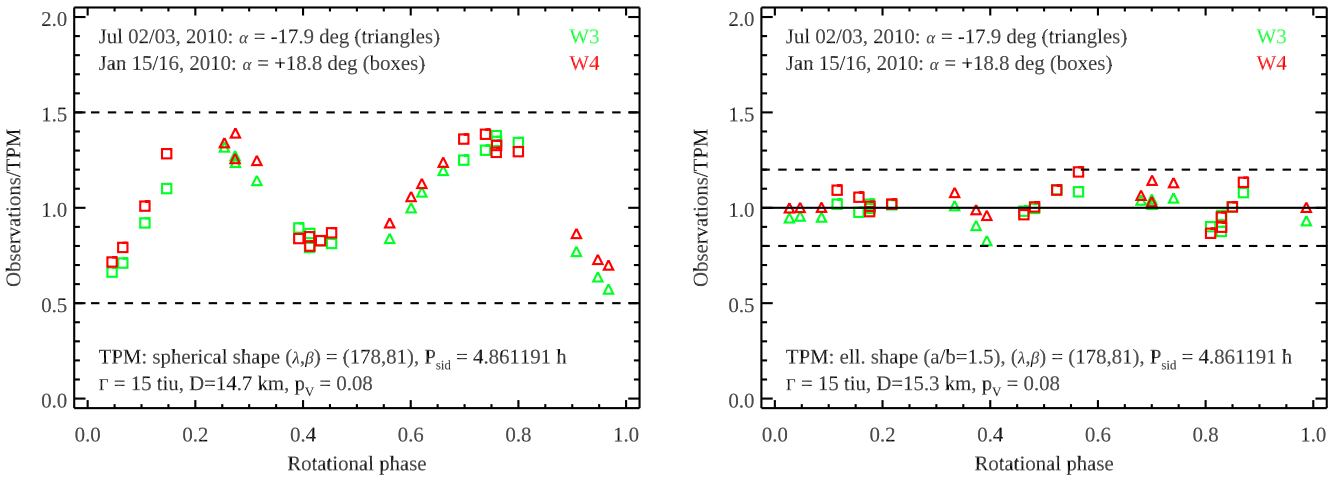


**Fig. B.1.** WISE W3 and W4 data from 2010 from both epochs before and after opposition. Left: WISE observations divided by a TPM prediction assuming a spherical shape. Right: Same, but divided by a TPM prediction assuming an ellipsoidal shape with a/b = 1.5. For both figures we take the same spin and thermal properties into account.